

## Full length article

# Dependence of hydrogen embrittlement mechanisms on microstructure-driven hydrogen distribution in medium Mn steels

Binhan Sun\*, Waldemar Krieger, Michael Rohwerder, Dirk Ponge\*, Dierk Raabe

Max-Planck-Institut für Eisenforschung GmbH, Max-Planck-Straße 1, 40237 Düsseldorf, Germany

## ARTICLE INFO

## Article history:

Received 2 August 2019

Revised 26 October 2019

Accepted 11 November 2019

Available online 14 November 2019

## Keywords:

Medium Mn steels

Hydrogen embrittlement

Hydrogen-enhanced decohesion (HEDE)

Hydrogen-enhanced local plasticity (HELP)

Hydrogen trapping

## ABSTRACT

The risk of hydrogen embrittlement (HE) is currently one important factor impeding the use of medium Mn steels. However, knowledge about HE in these materials is sparse. Their multiphase microstructure with highly variable phase conditions (e.g. fraction, percolation and dislocation density) and the feature of deformation-driven phase transformation render systematic studies of HE mechanisms challenging. Here we investigate two austenite-ferrite medium Mn steel samples with very different phase characteristics. The first one has a ferritic matrix (~74 vol.% ferrite) with embedded austenite and a high dislocation density ( $\sim 10^{14} \text{ m}^{-2}$ ) in ferrite. The second one has a well recrystallized microstructure consisting of an austenitic matrix (~59 vol.% austenite) and embedded ferrite. We observe that the two types of microstructures show very different response to HE, due to fundamental differences between the HE micro-mechanisms acting in them. The influence of H in the first type of microstructure is explained by the H-enhanced local plastic flow in ferrite and the resulting increased strain incompatibility between ferrite and the adjacent phase mixture of austenite and strain-induced  $\alpha'$ -martensite. In the second type of microstructure, the dominant role of H lies in its decohesion effect on phase and grain boundaries, due to the initially trapped H at the interfaces and subsequent H migration driven by deformation-induced austenite-to-martensite transformation. The fundamental change in the prevalent HE mechanisms between these two microstructures is related to the spatial distribution of H within them. This observation provides significant insights for future microstructural design towards higher HE resistance of high-strength steels.

© 2019 Acta Materialia Inc. Published by Elsevier Ltd. All rights reserved.

## 1. Introduction

During the last decade, medium Mn steels containing 3 to 12 wt.% Mn have received considerable attention, driven by the increasing demand for strong and compositionally lean materials with good formability from the automotive industry. The most widely investigated microstructure of this type of steels consists of ultrafine grained ferrite and austenite [1–4], realized by inter-critical annealing (IA). Different alloy compositions, starting microstructures before heat treatment as well as IA conditions can result in a wide range of microstructural characteristics, such as the austenite fraction (typically ranging from 20 to 70 vol.% [3–7]), grain size (from below 200 nm up to a few micrometers [3,4]), phase morphology (globular or laminated [2,6]), microstructure percolation and dislocation density [8]. Among these parameters, the fraction of austenite has a crucial influence on the me-

chanical properties of such steels. For a given alloy composition, a higher austenite fraction typically corresponds to a lower content of C and Mn partitioning into austenite, an effect which leads to lower austenite stability and an enhanced transformation-induced plasticity (TRIP) effect [4,5,7,9]. Most studies on such steels have focused so far on tailoring austenite conditions, in order to achieve an improved strength-ductility combination [3,5,7,10]. The tensile strength of austenite-ferrite medium Mn steels normally ranges from ~800 to 1400 MPa [2–4,10]. This high strength level fuels concerns about hydrogen embrittlement (HE), impeding the use of these steels.

At present, the knowledge of HE in medium Mn steels is very limited, with only a few reports published [1,2,9,11]. Ryu et al. [1] investigated the H desorption behavior and evaluated the HE susceptibility as a function of H concentration in two TRIP-assisted 5Mn (in wt.%) steels containing ~30 vol.% austenite. Han et al. [2] compared the HE behavior of a 0.1C-7Mn-0.5Si steel with two different phase morphologies (globular and laminated), focusing on the difference in the H-induced degradation of the tensile properties, H-assisted damage and the resulting fracture surfaces. Shao

\* Corresponding authors.

E-mail addresses: [b.sun@mpie.de](mailto:b.sun@mpie.de), [binhan.sun@mail.mcgill.ca](mailto:binhan.sun@mail.mcgill.ca) (B. Sun), [d.ponge@mpie.de](mailto:d.ponge@mpie.de) (D. Ponge).

et al. [9] and Zhang et al. [11] mainly addressed the influence of some processing parameters (e.g. intercritical annealing time and rolling methods) on the HE susceptibility of a Al-containing medium Mn steel. A clear picture of HE micromechanisms acting in medium Mn steels and the governing microstructural factors are currently not available.

The HE behavior in medium Mn steels is complex, due to three reasons: (1) The high contrast between ferrite and austenite in terms of H diffusivity and solubility [12–14] makes the H migration and trapping behavior in such steels more complicated than in materials consisting of a single phase or multiple phases with similar crystal structures (e.g. ferrite-martensite dual phase steels). (2) The austenite-ferrite interfaces are known as strong trapping sites for H [15,16]. The density and spatial arrangement of such planar defects thus affect H trapping and migration. (3) The austenite-to-martensite transformation occurring during deformation resets the local structure and micromechanical state in terms of strain/stress partitioning and localization [17,18], as well as the local thermodynamic driving forces for H migration [1]. These three factors imply that the change of phase conditions (e.g. fraction, percolation, mechanical stability) in such steels might significantly affect the H trapping and migration, the resulting HE susceptibility, and even the prevalent HE micromechanisms such as hydrogen-enhanced decohesion (HEDE) [19,20], hydrogen-enhanced local plasticity (HELP) [21–23] and adsorption-induced dislocation emission (AIDE) [24]. The former two mechanisms refer to the influence of internal H atoms in the bulk, whereas the AIDE model is based on H adsorption at the crack surface. Therefore, for obtaining a better understanding of the HE mechanisms in medium Mn steels, a more comprehensive investigation covering a more systematic range of phase conditions is required.

For the present study, we produced two austenite-ferrite microstructures in a medium Mn steel, covering a wide range of phase conditions. One has a ferritic matrix (~74 vol.%  $\alpha$ ) with embedded austenite, high austenite mechanical stability (absence of strain-induced martensite transformation during uniform straining), and a high dislocation density ( $\sim 10^{14} \text{ m}^{-2}$ ) in ferrite. The other one has an austenitic matrix (~59 vol.%  $\gamma$ ) with embedded ferrite, a low austenite stability (strain-induced martensite transformation occurs immediately after yielding), and a well recrystallized state. These two microstructural states lead to very different response to HE. The underlying mechanisms are discussed based on a systematic analysis of H trapping, H-assisted damage evolution (in both qualitative and quantitative manners), and H-assisted dislocation patterning and localization. Some supporting evidence based on the strain-rate dependence of the HE susceptibility is also given. In the last part of the study, the critical microstructural factors governing HE in medium Mn steels and the implications of the current study on future microstructural design are discussed.

## 2. Experimental procedure

We selected a model medium Mn steel with chemical composition 0.2C-10.2Mn-2.8Al-1Si (in wt.%). The relatively high Mn content ensures a large fraction of attainable austenite (above 50 vol.%), which allows microstructure tuning from a ferrite dominated matrix to an austenite dominated matrix. The addition of Al and Si serves to enlarge the intercritical domain thus realizing easier microstructural control. Casting, hot and cold rolling schedules have been described elsewhere [25] (the total thickness reduction by cold rolling is slightly higher here (~55%)). The cold rolled steel was subjected to intercritical annealing in a box furnace for 10 min, followed by water quenching. Two different IA temperatures (700 and 800°C) were selected to produce two profoundly different types of austenite-ferrite microstructures with 'extreme' (i.e. upper and lower bound) microstructural conditions in terms

of phase fraction, austenite mechanical stability and initial dislocation density. Based on a previous study on the same steel subjected to different annealing temperatures from 650 to 900 °C with a 50 °C interval [25], the two selected IA temperatures (700 and 800°C) correspond to the minimum and maximum austenite fraction, respectively, without carbides or quenched martensite formation. The samples intercritically annealed at 700 and 800°C are referred to as IA700 and IA800 hereafter.

The HE susceptibility of the two intercritically annealed samples were evaluated by slow strain rate tensile testing with an initial strain rate of  $\sim 8 \times 10^{-5} \text{ s}^{-1}$ . Tensile experiments were conducted using a Kammrath & Weiss stage coupled with the digital image correlation (DIC) technique. A tensile specimen with gage length of 4 mm, gage width of 1.8 mm and thickness of ~1.1 mm was used. Global and local strains were measured by DIC. Hydrogen charging was performed electrochemically in an aqueous solution containing 3 wt.% NaCl and 0.3 wt.%  $\text{NH}_4\text{SCN}$  at a current density of 5 A/m<sup>2</sup>. A platinum foil was used as the counter electrode and the charging time was 24 h. The time interval between the end of H pre-charging and the start of tensile testing was less than 15 min. The total time elapsed during the slow strain rate tensile testing is around 75 and 60 min for the H pre-charged IA700 and IA800 specimens, respectively. The H loss during this short time period is considered to be very small for the investigated samples, since no substantial H desorption was detected for the H-charged IA700 sample even after exposing it to atmosphere at ambient temperature for a much longer time period of 24 h.

The H concentration and trapping behavior of the H-charged samples were studied by thermal desorption analysis (TDA) conducted using a proprietary Ultra High Vacuum based set-up [26]. The gases evolving during the continuous heating of a sample were detected by an MKS MicroVision 2 quadrupole mass spectrometer. The sample size for TDA was about 15 mm  $\times$  15 mm  $\times$  1.1 mm, and the H charging condition for TDA samples was the same as for the tensile specimens mentioned above. The first set of TDA experiments was carried out within 15 min after H charging. The total concentration of H was determined by measuring the cumulative desorbed H from room temperature to 800°C, subtracted by the value of a reference non-charged sample. A Kissinger analysis [27,28] was applied in order to determine the activation energy ( $E_A$ ) for hydrogen desorption from different trapping sites. For this, TDA spectra were measured at different heating rates ( $\Phi$ ) ranging from 6.5 to 90 °C/min. The TDA set-up was previously calibrated within this heating rate range [26]. The activation energy was calculated from the following equation [26,29]:

$$-E_A/R = d \ln(\Phi/T_{\max}^2) / d(1/T_{\max})$$

where  $T_{\max}$  is the temperature corresponding to the maximum value of each desorption peak and  $R$  is the gas constant. The second set of the TDA experiments was conducted for the samples which were charged and then aged under vacuum (pressure  $\sim 10^{-3} \text{ Pa}$ ) at ambient temperature for different time intervals (48 to 120 h). The aging process was to desorb H from some weaker traps (i.e. disappearance of low temperature TDA peaks), enabling clearer identification of different H trapping sites.

The microstructure, damage (voids or cracks) and fracture surface of the samples with and without H pre-charging were characterized by a combined use of secondary electron (SE) and backscattered electron (BSE) imaging (Zeiss-Crossbeam XB 1540 FIB-SEM instrument), electron backscatter diffraction (EBSD, JEOL JSM-6500F SEM) and electron channeling contrast imaging (ECCI, Zeiss-Merlin SEM). The combination of these characterization techniques ensures both a high spatial resolution (sufficient to probe single dislocations in ECCI mode [30,31]) and good statistics. Quantification of the phase fraction and grain size was conducted by the TSL OIM software package, based on the EBSD data

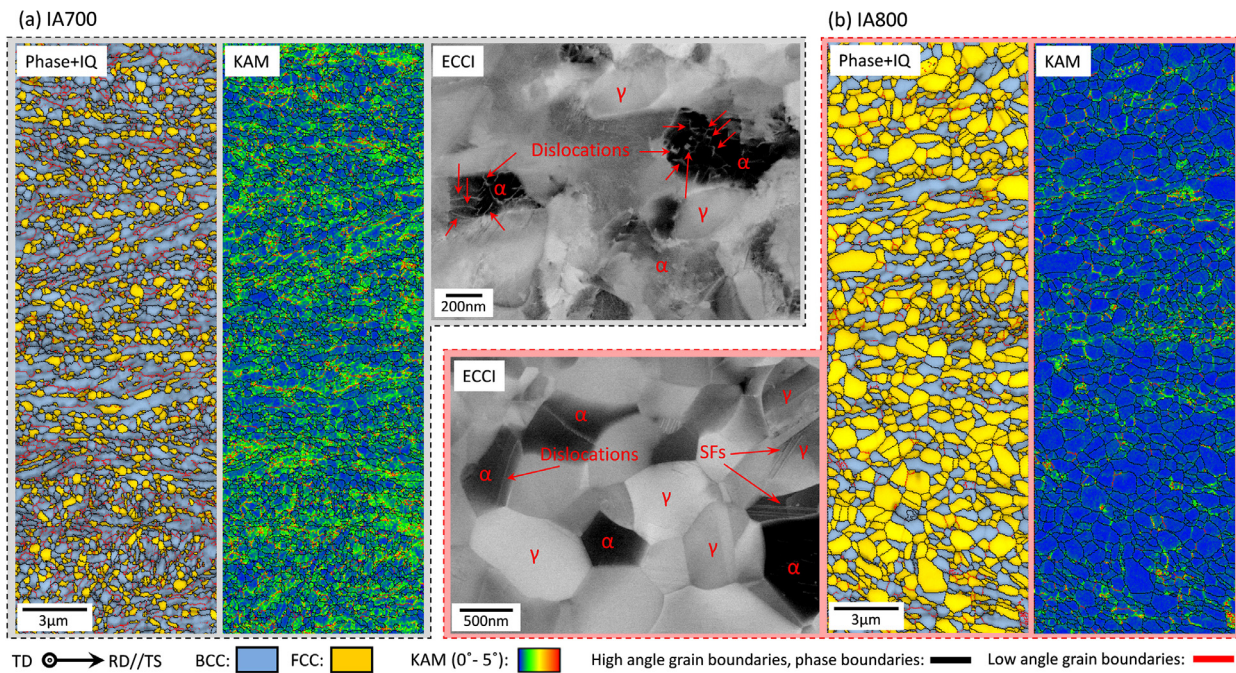


**Fig. 1.** EBSD phase, image quality (IQ) and kernel average misorientation (KAM) mapping and electron channeling contrast imaging (ECCI) of a higher magnification for (a) the IA700 sample and (b) the IA800 sample. (Some of the dislocations and stacking faults (SFs) are marked by arrows.) (For interpretation of the references to color in this figure legend, the reader is referred to the web version of this article.)

**Table 1**

Microstructural details (phase fraction, grain size,  $M_s$  and  $M_{d_{30}}$  temperatures, dislocation density and the kernel average misorientation (KAM) value of ferrite) of the two intercritically annealed samples and their H concentration after electrochemical charging for 24 h.

Sample	Austenite fraction (vol.%)	Grain size (nm)		$M_s^a$ (°C)	$M_{d_{30}}^b$ (°C)	Dislocation density of ferrite ( $m^{-2}$ )	KAM of ferrite (deg.)	H concentration (wt ppm)
		$\gamma$	$\alpha$					
IA700	26.0	260	470	<−90	285.1	$1.0 \times 10^{14}$	0.81	15.5 (4.9) <sup>c</sup>
IA800	59.3	530	500	−49.6	347.3	$7.5 \times 10^{12}$	0.47	6.3 (1.5) <sup>c</sup>

<sup>a</sup> The  $M_s$  temperatures for the two samples were measured using a dilatometer (DIL 805A/D) upon continuous cooling from room temperature to −90 °C at a cooling rate of 6 °C/min; no obvious phase transition points have been detected for the IA700 sample down to −90 °C.

<sup>b</sup>  $M_{d_{30}}$  is the temperature at which half of the austenite is transformed to martensite after a strain of 30%; it was calculated based on the empirical equation described in Ref. [17] and austenite compositions calculated using the Thermo-Calc software with the TCFe7 database.

<sup>c</sup> Values given in parentheses are the standard deviations from more than 7 measurements.

containing a large probing area with more than ~2000 grains. The average density of dislocations was estimated based on the ECCI observation of ~50 individual grains for each sample (more details can be found elsewhere [32]). Transmission Kikuchi diffraction (TKD, Zeiss-Merlin SEM with an OPTIMUS<sup>TM</sup> TKD Detector) was conducted to provide nanoscale imaging of local misorientations for deformed specimens with and without H pre-charging. The step size for TKD was 5 nm. Samples for TKD were prepared by focused ion beam (FIB) lift-out techniques using a dual beam SEM/FIB instrument (FEI Helios Nanolab 600i).

### 3. Results

#### 3.1. Microstructure and hydrogen trapping behavior

The microstructure of the two intercritically annealed samples are shown in Fig. 1, with more detailed information (e.g. phase fraction, grain size,  $M_s$  and  $M_{d_{30}}$  temperatures, dislocation density and the kernel average misorientation (KAM) value of ferrite) listed in Table 1. Both samples develop an ultrafine austenite-ferrite microstructure after intercritical annealing (Fig. 1). The two samples exhibit very different microstructural characteristics. The IA700 has a ferritic matrix (74 vol.%  $\alpha$  and 26 vol.%  $\gamma$ ). The low austenite volume fraction leads to a high amount of C and Mn partitioning into

the austenite, as predicted by Thermo-Calc simulations and experimentally validated in previous studies [4,25]. This results in a high thermal and mechanical stability of austenite (i.e. the  $M_s$  is below −90 °C and the  $M_{d_{30}}$  temperature was calculated to be 285.1 °C, Table 1), which prevents strain-induced martensite transformation during uniform straining (will be shown in Section 3.2). The static recrystallization of ferrite in the IA700 sample is not complete due to the low IA temperature, which is reflected by the high kernel average misorientation (KAM) value (Fig. 1(a) and Table 1). The average dislocation density in ferrite is thus high (as revealed by ECCI in Fig. 1(a)), with the value estimated to be  $\sim 10^{14} m^{-2}$  (Table 1). In contrast, the IA800 sample shows an austenitic matrix (59 vol.%  $\gamma$ ) and a well recrystallized microstructure with only a few dislocations and stacking faults (Fig. 1(b)). The lower C and Mn enrichment in austenite along with its larger grain size (530 nm vs. 260 nm in the IA700 sample) give rise to lower austenite stability (i.e.  $M_s = -49.6$  °C and  $M_{d_{30}} = 347.3$  °C, Table 1).

The hydrogen desorption spectra for the two samples with and without aging at a continuous heating rate of 26 °C/min are shown in Fig. 2(a). After H charging, the IA700 sample contains a much higher H concentration than the IA800 sample (15.5 wt ppm vs. 6.3 wt ppm, Table 1). Since austenite has a much higher H solubility than ferrite (about 2 orders of magnitude higher [12]), this observation suggests that H does not saturate at least in the



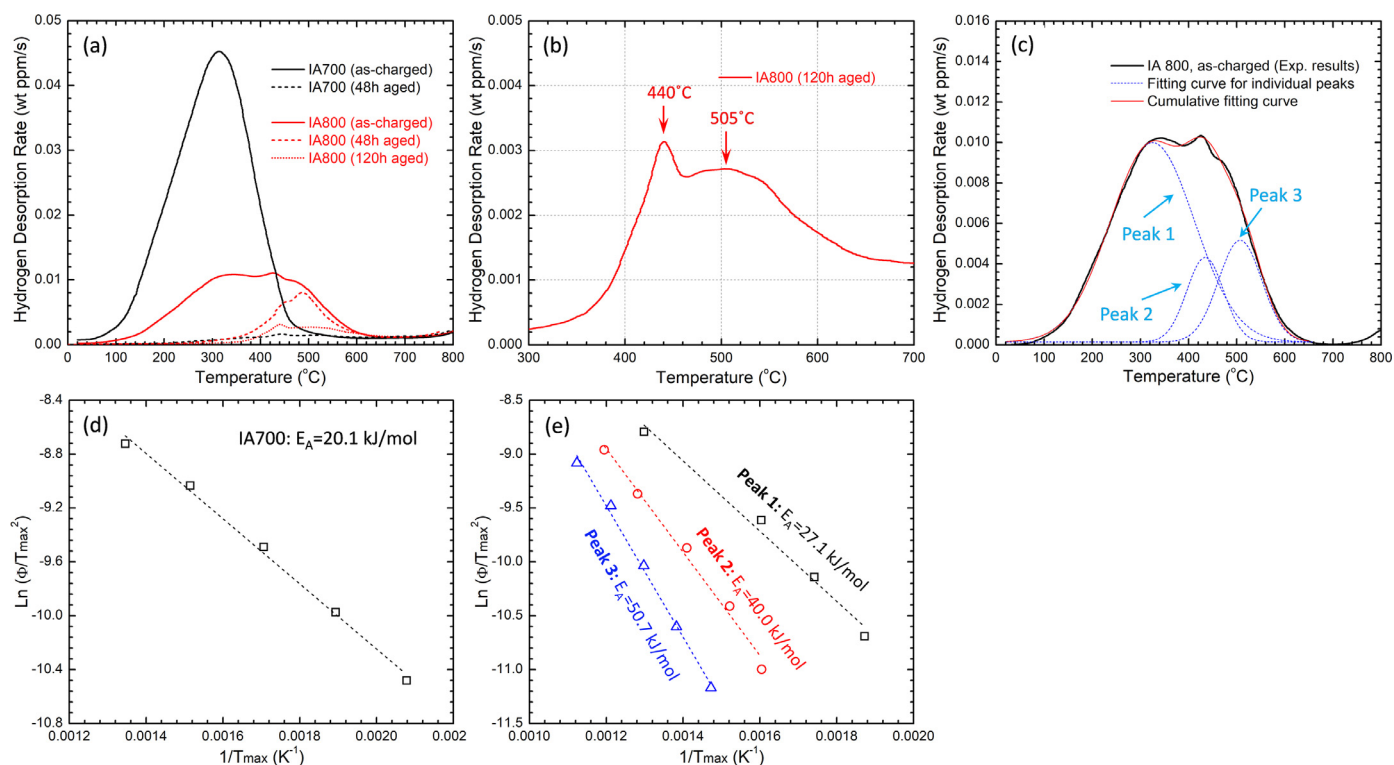


**Fig. 2.** (a) Hydrogen desorption spectra of the two intercritically annealed samples with and without aging at a heating rate of 26 °C/min; (b) Magnified TDA spectrum of the IA800 sample subjected to electrochemical charging followed by room-temperature aging for 120 h under vacuum; (c) Multi-peak fitting results for the as-charged IA800 sample; Kissinger plot ( $\ln(\Phi/T_{max}^2)$  vs.  $1/T_{max}$ ) for the as-charged (d) IA700 sample and (e) IA800 sample. (The dash lines in (d) and (e) are the fitting curves based on linear regression. The Pearson correlation coefficients for all the linear fitting are above 0.99.)

IA800 sample. In addition, the as-charged IA700 sample shows only one desorption peak with the peak temperature located at around 315°C (Fig. 2(a)), whereas multiple peaks can be found for the IA800 sample with some peaks positioned above 400°C. After room temperature aging for 48 h under vacuum, the peak of the IA700 sample disappears meaning that almost all the charged H detraps and diffuses out. However, there is still some H remaining in the IA800 sample (~1.9 wt ppm) after 48 h aging, which does not totally diffuse out even after 120 h aging (~0.7 wt ppm remaining). These observations strongly suggest that in the IA800 sample, some of the charged H remains trapped at strong trapping sites. It has been defined that ‘diffusible H’ is the fraction of the total H content which can diffuse out at ambient temperature [16,33]. In this regard, it should be noted that the remaining H in the IA800 sample after 120 h aging can still be regarded as diffusible, since it would eventually diffuse out after aging for longer times.

We next analyze the activation energies associated with the desorption peaks and use this information to deduce the H trapping behavior in the two specimens. For the IA700 sample, the relatively low peak temperature and the disappearance of the desorption peak after aging suggest that most of the H is trapped in relatively weak trapping sites. The desorption activation energy determined for this peak is around 20 kJ/mol (Fig. 2(d)), which is similar to the range reported for H trapping at dislocations or grain boundaries in ferrite ( $E_A = 17\text{--}33$  [29,34–36], determined by TDA). Other possible H trapping sites (e.g. iron-vacancy, microvoids, inclusions, austenite and austenite-ferrite interface) might in principle also contribute to this peak, but they are not assumed to be prevalent here owing to their higher H trapping energies ( $E_A$  normally above 35 kJ/mol [1,15,16,35,37,38]).

The H trapping state in the IA800 sample is more complex as indicated by the multiple peaks visible in the desorption spectrum (Fig. 2(a)). The peaks need to be separated before evaluating their

associated activation energy values. Fig. 2(b) reveals that two small but distinct desorption peaks appear for the IA800 sample after 120 h aging. These two peaks center at around 440 and 505 °C (at the heating rate of 26 °C/min), respectively. With the aid of this information, peak separation was conducted using Gaussian fitting [39], identifying three major peaks, as shown in Fig. 2(c). The first peak has its maximum at ~325 °C which is very close to the peak position of the IA700 sample (~315 °C). This finding suggests that this peak could be due to H detrapping from the same types of sites, i.e. dislocations and/or grain boundaries in ferrite. This point is supported by the fact that the peak almost disappears after 48 h aging in both materials (Fig. 2(a)). The  $E_A$  determined for the first peak is ~27 kJ/mol (Fig. 2(e)), slightly higher than the value of the peak in the IA700 sample. This difference could be due to the higher contribution of the H diffusion activation energy in the IA800 sample containing a higher fraction of austenite, given that  $E_A$  is a combination of the H binding energy ( $E_b$ ) and the H diffusion activation energy ( $E_{diff}$ ) [16,29,35]. The desorption activation energy for the second and third peak of the IA800 sample was determined to be ~40 and ~51 kJ/mol (Fig. 2(e)), respectively. Possible associated H trapping mechanisms in this sample will be further discussed in Section 4.1, combined with the mechanical results and the damage analysis.

### 3.2. Influence of hydrogen on the mechanical properties

The tensile behavior and the austenite fraction change due to strain-induced  $\alpha'$ -martensite formation for the two samples with and without H pre-charging are shown in Fig. 3. The detailed mechanical properties are listed in Table 2. For the non-charged IA700 sample, the smaller grain size and initially high dislocation density in the ferrite give rise to a high yield strength (~1166 MPa, Fig. 3(a) and Table 2). However, the austenite in



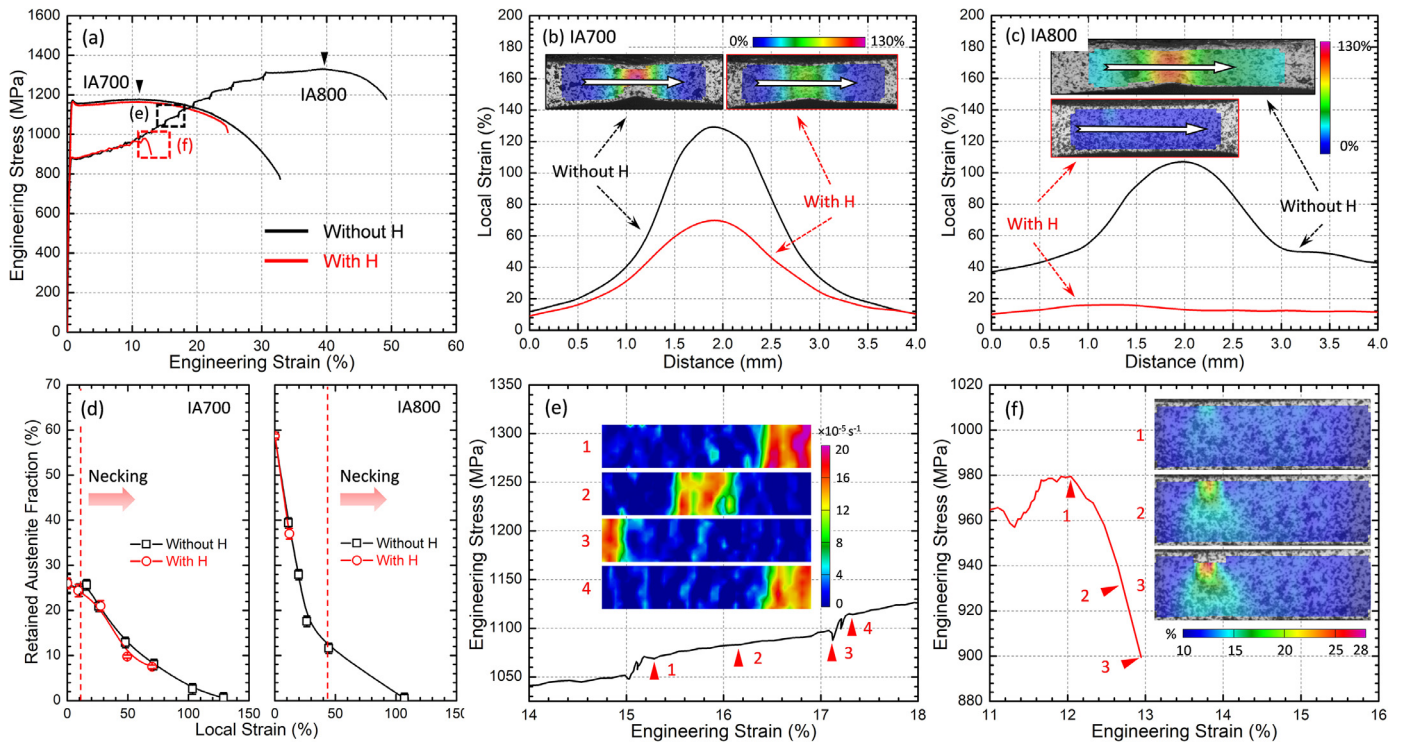


**Fig. 3.** (a) Engineering stress-strain curve of the two intercritically annealed samples with and without H pre-charging (the strain at the point of ultimate tensile strength (i.e. uniform strain/elongation) for each tensile curve is marked by a triangular symbol); Local tensile strain just prior to the fracture point as a function of sample distance (measured by DIC) for (b) the IA700 sample and (c) the IA800 sample with and without H pre-charging (the corresponding strain maps are also inset, with the white arrows showing the areas where the strain profiles were taken); (d) Change of austenite fraction (measured by EBSD) as a function of local strain for the two samples with and without H pre-charging (the strain corresponding to the onset of necking is marked by dash lines). The corresponding EBSD maps are shown in the **Supplementary Material**; (e) Magnified tensile curve for the IA800 sample without H (taken from the black rectangular frame in (a)) and the corresponding strain rate maps showing the propagation of one PLC band; (f) Magnified tensile curve for the IA800 sample with H (taken from the red rectangular frame in (a)) and the corresponding strain maps showing the macroscopic crack nucleation and propagation. (For interpretation of the references to color in this figure legend, the reader is referred to the web version of this article.)

**Table 2**

Details about the mechanical properties of the two intercritically annealed samples with and without H pre-charging, subjected to slow strain rate tensile testing (values in the parentheses are the standard deviations from more than two repeating experiments).

Sample		Yield strength (MPa)	Tensile strength (MPa)	Uniform elongation (%)	Post-uniform elongation (%)	Total elongation (%)	Local strain in the necking area prior to fracture (%)	Total elongation loss due to H (%)
IA700	Without H	1165.7 (24.8)	1171.1 (23.4)	10.6 (0.4)	21.0 (1.6)	31.6 (1.2)	129.2 (4.5)	8.5
	With H	1161.4 (13.8)	1160.3 (15.1)	9.6 (1.1)	13.5 (0.6)	23.1 (1.7)	67.6 (3.7)	
IA800	Without H	891.7 (12.4)	1327.0 (3.9)	40.8 (1.4)	10.3 (0.4)	51.1 (1.8)	101.8 (3.0)	38.2
	With H	895.7 (10.7)	991.3 (11.8)	12.1 (0.1)	–	12.9 (0.1)	–	

this sample is relatively stable, so that it does not transform to  $\alpha'$ -martensite during uniform straining, as shown in Fig. 3(d). Deformation-induced austenite-to-martensite transformation only occurs during necking (Fig. 3(d)), promoted by strain localization and stress triaxiality in the necking area [40]. Such a late-stage onset of the TRIP effect results in a low work hardening rate, low ultimate tensile strength ( $\sim 1171$  MPa) and low uniform elongation ( $\sim 10.6\%$ ), but a high resistance to fracture in the necking regime and thus high post-uniform elongation ( $\sim 21\%$ ). The influence of the austenite mechanical stability on work hardening and fracture tolerance in similar steels have been the subject of previous works [4,17]. In contrast, the non-charged IA800 sample shows a lower yield strength ( $\sim 892$  MPa) due to the larger average grain size and almost fully recrystallized microstructure. The austenite is rather metastable and thus transforms to  $\alpha'$ -martensite already at the beginning of tensile straining (Fig. 2(d)). The early-stage TRIP effect is responsible for the material's higher work hardening rate, higher tensile strength ( $\sim 1327$  MPa) and uniform elongation ( $\sim 40.8\%$ ), as well as the lower post-uniform elongation ( $\sim 10.3\%$ )

[17]. In addition, the IA800 sample shows a serrated flow behavior which is characterized by the intermittent nucleation of localized bands followed by their continuous propagation during tensile straining (Fig. 3(e)). This phenomenon has been referred to as the Portevin-Le Chatelier (PLC) effect and is normally attributed to dynamic strain aging (DSA) in single phase materials [41–43].

For both samples, the presence of H does not affect the yield strength (Fig. 3(a) and Table 2), rate of strain-induced martensite formation (Fig. 3(d)) and strain hardening rate (Fig. 3(a)). In the case of the IA700 sample, the uniform elongation is very similar for the non-charged and H pre-charged conditions (Fig. 3(a) and Table 2), only the post-uniform elongation is reduced due to the presence of H (Table 2). This is also reflected in the local strain profiles shown in Fig. 3(b). The H pre-charged IA700 sample exhibits a much lower local strain value ( $\sim 68\%$ ) in the necking area just before fracture compared with the non-charged sample ( $\sim 129\%$ ), whereas the values outside the necking area are almost identical. This means that the presence of H in the IA700 sample only affects the necking regime by influencing the damage

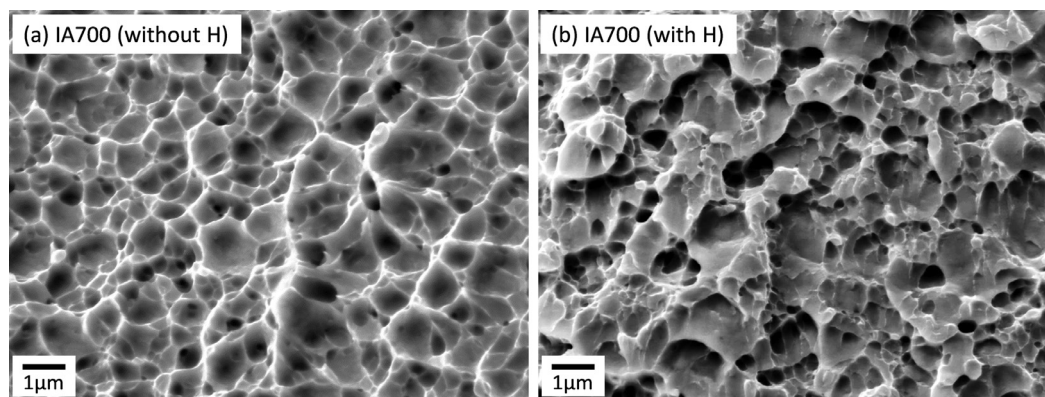


Fig. 4. Typical SEM fractograph of the IA700 sample (a) without H pre-charging and (b) with H pre-charging.

evolution. The tensile strength of this sample is thus not affected by H (Fig. 3(a) and Table 2).

However, for the H pre-charged IA800 sample, fracture occurs at about 13% strain, well before necking (i.e. in the uniform strain stage). The local strain profile of this sample (Fig. 3(c)) also shows the absence of necking. Therefore, both the tensile strength and ductility of the IA800 sample are reduced by the presence of H (Fig. 3(a) and Table 2). A sudden stress drop has been observed at the end of the tensile curve just prior to fracture, as marked by a rectangular frame and magnified in Fig. 3(f). This is due to the nucleation of a macroscopic crack at one edge of the tensile specimen, followed by its propagation to the center part until catastrophic fracture occurs (as revealed by the DIC results in Fig. 3(f)).

Nevertheless, the results clearly show that the IA700 sample, although loaded with a much higher H concentration and equipped with a higher yield strength, shows a much lower H-induced reduction of the total elongation compared to the IA800 sample (8.5% for IA700 vs. 38.2% for IA800, Table 2). This observation provides a distinct evidence showing that the IA700 sample has a much higher resistance to HE than the IA800 sample.

### 3.3. Influence of hydrogen on the damage behavior

#### 3.3.1. Sample IA700 with ferritic matrix

The typical SEM fractograph of the IA700 sample with and without H pre-charging is shown in Fig. 4. Both samples exhibit a major dimple-type behavior throughout the whole fracture surface, with the size of most dimples below  $1\ \mu\text{m}$  (Fig. 4(a) and (b)). However, the dimples in the H-charged IA700 sample are much shallower than those in the non-charged condition. We next analyze the damage near the fracture surface of the cross-sectioned tensile samples. The results are shown in Fig. 5. For both, non-charged and H pre-charged IA700 samples, the fracture is mainly driven by void formation during the necking stage. Three types of void nucleation sites are identified regardless of H pre-charging (Fig. 5(a) and (b)): at interfaces between  $\alpha$  and  $\gamma/\alpha'$ , inside  $\gamma/\alpha'$  and inside  $\alpha$ . We note that although the austenite near the fracture surface of the non-charged IA700 sample has completely transformed to  $\alpha'$  (Fig. 3(d)), it is not certain whether the voids form prior to or after  $\alpha'$ -martensite formation. Thus here we use  $\gamma/\alpha'$  rather than  $\alpha'$  to describe the void formation sites. In order to identify the preferred void nucleation site, we establish a statistical analysis by analyzing all the visible voids adjacent to the fracture surface. The number of analyzed voids are  $\sim 100$  and  $\sim 150$  for the non-charged and H pre-charged sample, respectively. The proportion of different void formation sites (equals the number of voids from specific sites divided by the total void number) for the two samples is shown in Fig. 5(c). The analysis shows that the pres-

ence of H in the IA700 sample does not alter the prevalent void formation site, which is the  $\alpha$ - $\gamma/\alpha'$  interface with a proportion of  $\sim 85\%$  for both the H-charged and non-charged states.

It is important to mention that the  $\alpha$ - $\gamma/\alpha'$  interface in this sample should not be intrinsically weak even after H charging, since neither damage propagation along the interface nor an intergranular fracture mode was observed. The interfacial void nucleation is thus believed to be due to the strain incompatibility between  $\alpha$  and the adjacent  $\gamma$ - $\alpha'$  mixed phase, resulting from their mechanical contrast. Such mechanical contrast and the resulting strain incompatibility are gradually even increased with the progressive formation of  $\alpha'$ -martensite during deformation. The associated plastic deformation mismatch is essentially accommodated by high densities of geometrically necessary dislocations (GNDs) in the interface regions [25,44], which increases the local stress concentration (or back stress) and promotes void nucleation [45,46]. This can be observed in Fig. 5(d) and (e), which show ECCI results of the H pre-charged IA700 sample taken from two typical areas with a local strain of  $\sim 48\%$ . In both regions, one ferrite grain (marked by red dashed lines) is in approximate channeling contrast condition. Inside these two particular ferrite grains, the local regions near the interfaces and the voids appear bright, suggesting the presence of a high number of dislocations [30,31].

In order to further explore the influence of H, we performed a quantitative analysis of the deformation-induced damage evolution on both H-charged and non-charged IA700 samples. We used post-mortem high-resolution BSE imaging to probe damage events at different local strain levels (measured by DIC) in tensile fractured specimens [33]. Various types of damage-related information have been acquired by the statistical analysis of such BSE images containing tens to thousands of voids throughout the whole cross-section area at different strain levels. The information includes: (a) the number density of voids (void number divided by the total detection area) providing information about void nucleation; (b) the apparent void size which informs about void growth and/or coalescence and (c) the total void area fraction. The results are shown in Fig. 6. For both samples, the void number density starts to increase at strain levels above  $\sim 10\%$  which corresponds to the onset of necking. It continuously increases with local strain, followed by a finally dramatic rise at locations very near to the fracture surface (Fig. 6(a)). It is found that the H-charged specimen has a much higher void density (up to  $\sim 13$  times higher) compared to the non-charged sample. This phenomenon suggests that the void nucleation rate in sample IA700 is dramatically increased by the presence of H, namely by up to a factor of  $\sim 13$ .

The size of the voids in both samples is small (Fig. 5 and Fig. 6(b)). For the non-charged condition, the average void diameter increases from  $\sim 150\ \text{nm}$  at the onset of necking ( $\sim 10\%$  local



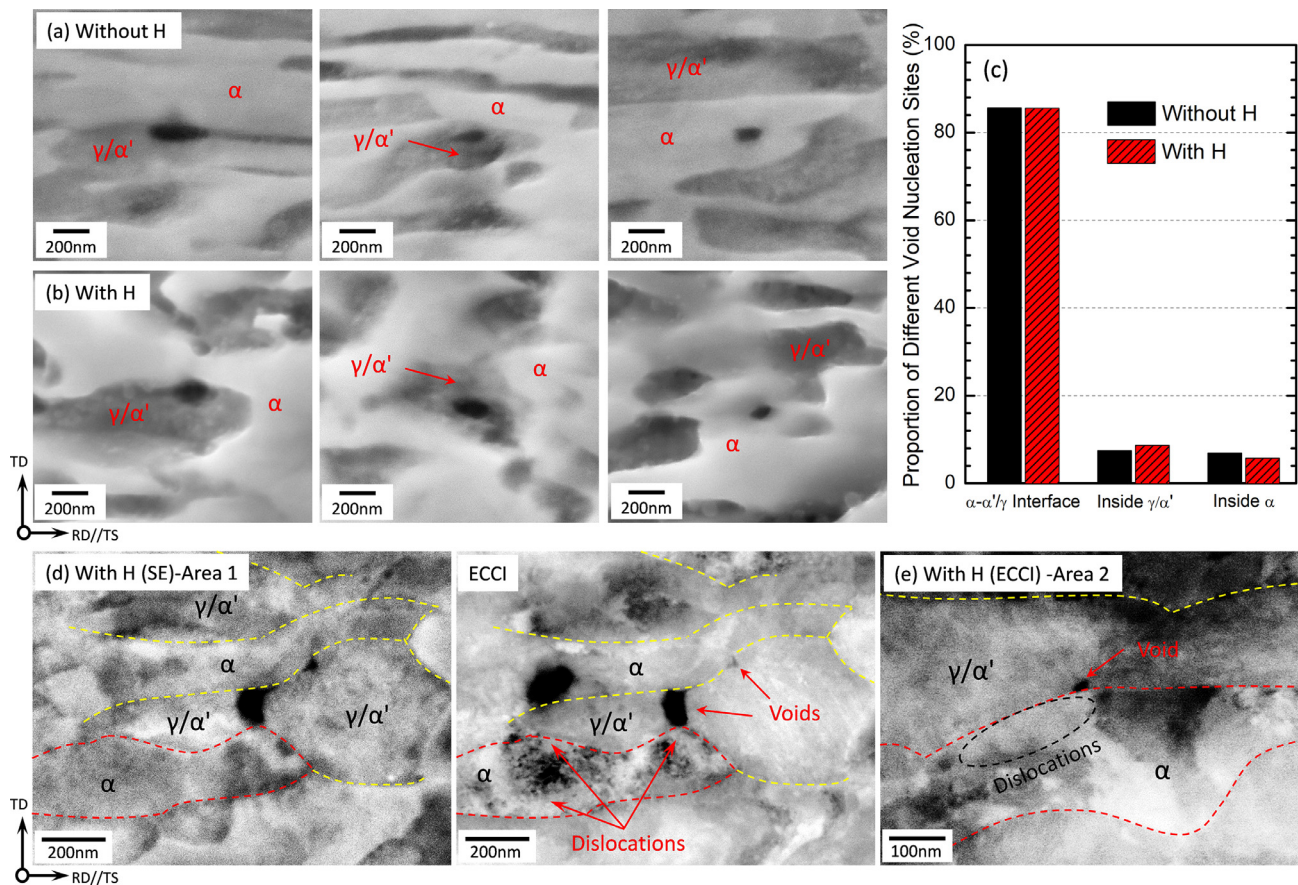


**Fig. 5.** Secondary electron (SE) images taken from locations near the fracture surface, showing void formation at different sites in the IA700 sample (a) without H pre-charging and (b) with H pre-charging (samples here were slightly etched by 1% nital); (c) Quantitative analysis of more than 100 voids near the fracture surface, showing the proportions of different void formation sites; (d) and (e) ECCI observations taken from two areas located at  $\sim 600 \mu\text{m}$  away from the fracture surface (local strain here is  $\sim 48\%$ ) of the H pre-charged IA700 sample, showing the typical  $\alpha$ - $\gamma/\alpha'$  interfacial voids and the nearby dislocation activities (the SE image in (d) serves to provide a more clear visualization of voids; the identification of different phases was supported based on their slight difference in topography due to mechanical polishing (revealed by SE imaging) and their different Mn concentrations (measured by Energy-Dispersive X-Ray Spectroscopy (EDX) line analysis)).

strain) to  $\sim 200 \text{ nm}$  in regions directly adjacent to the fracture surface ( $\sim 130\%$  local strain, Fig. 6(b)). This value is much smaller compared to other advanced high strength steels (e.g. dual phase [47] and high Mn steels [48,49]) where the reported damage size is of the order of a few micrometers. It is interesting to find that the average void size is even smaller in the H-charged specimen compared to the same material in non-charged condition at the same local strain (except at the highest strain point, Fig. 6(b)). However, Fig. 6(b) might not be suited to analyze the influence of H on void growth and/or coalescence as the average void size is calculated based on both newly nucleated voids and the voids which have already undergone some growth and/or coalescence. The much higher void nucleation rate in the H-charged sample would essentially contribute to a lower statistically averaged void size. For comparing the void growth and/or coalescence between the H-charged and non-charged IA700 samples, we average only the largest 20 voids at each local strain, assuming that these voids have not been newly nucleated [48]. The results are plotted in Fig. 6(c). We find that the average size of the largest 20 voids is quite comparable for the material in H-charged and non-charged state, except for the highest strain point of the H-charged sample ( $\sim 68\%$  local strain) where a more severe void coalescence could in principle occur due to the higher density of voids promoted by H (Fig. 6(a)). This observation suggests that H in the IA700 sample does not promote void growth. We can thus conclude that the early fracture of the H-charged IA700 sample is mainly due to the

dramatically increased (up to a factor of  $\sim 13$ ) void nucleation rate, which greatly increases the total fraction of damages (as shown in Fig. 6(d)).

### 3.3.2. Sample IA800 with austenitic matrix

Comparing to the IA700 sample where H has major influence on void formation and accumulation, the influence of H on the damage evolution in sample IA800 is completely different. We again start the analysis from the fracture surface (as shown in Fig. 7). The non-charged IA800 sample shows a dimple-type fracture surface (Fig. 7(f)), driven by void formation mainly at the  $\alpha$ - $\gamma/\alpha'$  interfaces, similar to the non-charged IA700 sample (the data for sample IA800 is not presented here for the purpose of conciseness). In contrast, the fracture surface of the H pre-charged IA800 specimen contains three zones with different fracture features (Fig. 7(a)). Zone I is the region just beneath the macroscopic crack observed by DIC (as shown in Fig. 3(f)). It is thus the part that is fractured first. A predominantly intergranular fracture is observed in this zone (Fig. 7(c)). The size of the intergranular facets is similar to the grain size of austenite and ferrite ( $\sim 500 \text{ nm}$ , Table 1). Zone II is a transition area containing both intergranular facets and dimples, as marked respectively by arrows and elliptical frames in Fig. 7(d). Zone III is the final ruptured region and shows a mainly dimple-type fracture appearance similar to the non-charged specimen (Fig. 7(e) and (f)). A statistical damage analysis along the whole cross-section at regions adjacent to the fracture surface



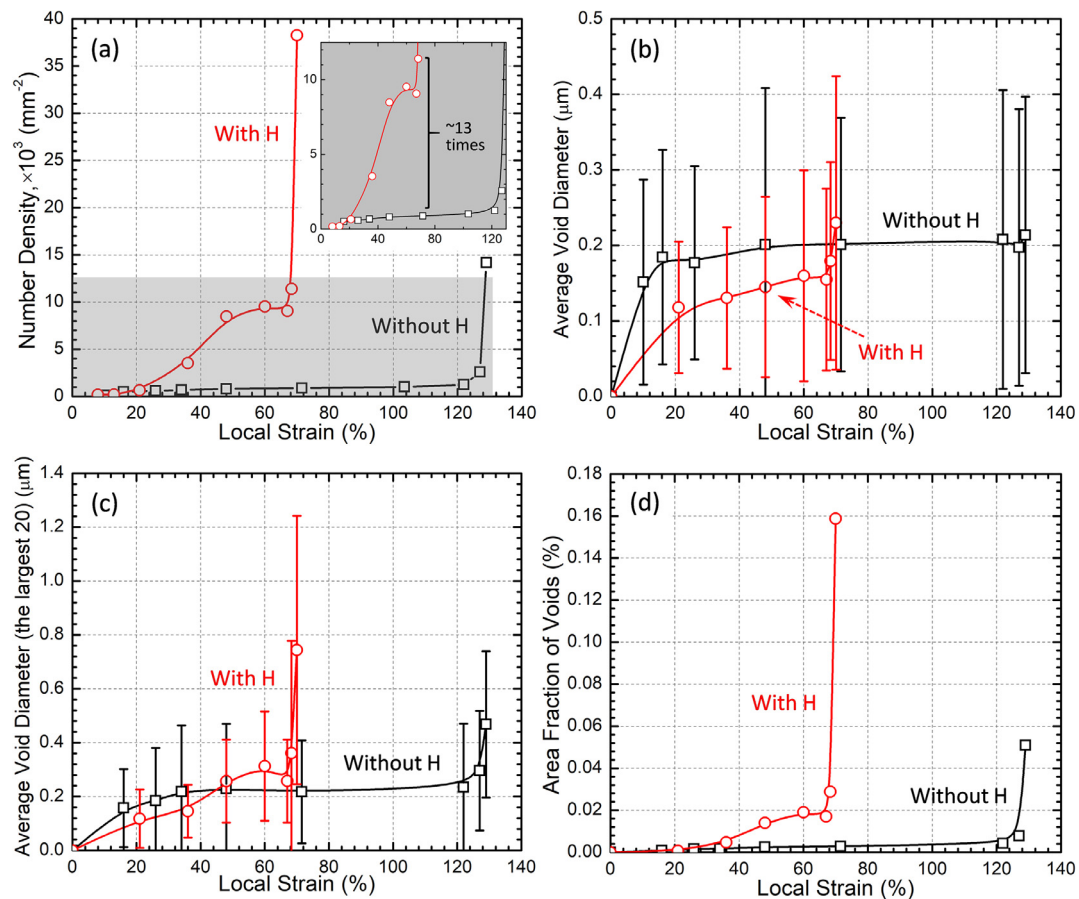


**Fig. 6.** (a) The number density of voids, (b) the average void size, (c) the average void size for the largest 20 voids and (d) the area fraction of voids as a function of local tensile strain in the IA700 samples with and without H pre-charging. (One magnified curve taken from the gray area is inset in (a)). The local strain was measured by DIC. The number density is defined as the counted void number divided by the total detecting area. The apparent void size was calculated assuming a sphere shape of the voids, and the equivalent diameter was taken. The void area fraction was calculated based on the void density and average area of voids measured by the Image J software.).

shows that the major damage characteristics in Zone I and Zone III consists in nano-/micro-cracking and void formation, respectively. The number density of damage incidents is remarkably increased from Zone I ( $10^3$ – $10^4$   $\text{mm}^{-2}$ ) to Zone III ( $1.2$ – $5.5 \times 10^4$   $\text{mm}^{-2}$ , Fig. 7(b)).

Nevertheless, it is evident that the H-assisted cracking behavior in Zone I is the cause for the fracture of the H pre-charged IA800 sample. Its investigation is thus the next focus and the results are shown in Figs. 8 and 9. Near this fracture zone, crack formation at different interface boundaries was frequently observed, which corresponds to the intergranular fracture behavior (Fig. 7(c)). The cracking events can be divided into two major groups: phase boundary cracking (Type I, Fig. 8(a) and (b)) and austenite or prior-austenite grain boundary cracking (Type II, Fig. 8(c)). They are summarized schematically in Fig. 8(d). Type I cracks are found either at the interfaces between ferrite and strain-induced  $\alpha'$ -martensite (Fig. 8(a)) or at austenite-ferrite interfaces (Fig. 8(b)). Note that some portion of the observed strain-induced  $\alpha'$ -martensite can be a consequence of the advancing  $\alpha$ - $\gamma$  interface cracking due to the resulting high stress/strain concentrations near the crack tips. This point is supported by (1) the ECCI results shown in Fig. 8(a) and (b) where a high density of dislocations is observed near the nanoscaled cracks, and (2) the EBSD results in Fig. 8(b) where the formation of  $\alpha'$ -martensite is observed near the interface crack tip. On the other hand, all the probed type II cracks (more than 15 imaged by EBSD) have a same feature, namely, all the austenite regions near the crack have transformed into  $\alpha'$ -martensite (as shown in Fig. 8(c)). This observation indi-

cates that type II cracking occurs after martensite formation and its propagation is thus along the prior-austenite grain boundaries (BCC-BCC type). The promoting effect of strain-induced martensite transformation on H-induced cracking in the IA800 sample will be discussed in Section 4.2.2.

The respective proportion of the two cracking events is quantified based on a statistical analysis of about 150 nano-/micro-cracks near the fracture Zone I. The results are shown in Fig. 9(a). It shows that type I cracking possesses a higher proportion compared with type II cracking (56% vs. 38%, Fig. 9(a)). However, the two-dimensional EBSD mapping reveals that the total length of the  $\alpha$ - $\gamma$  interface is almost twice as large as that of the austenite grain boundary in the non-deformed IA800 sample (Fig. 1(b)). This means that the actual possibility of crack formation could be comparable for the two crack formation sites. This is supported by Fig. 9(b), which is a typical example of a crack formation site showing that one crack nucleated at a triple junction and propagates almost simultaneously along both, the  $\alpha$ - $\gamma$ / $\alpha'$  interface and the prior-austenite grain boundary.

## 4. Discussion

### 4.1. Hydrogen trapping behavior

The TDA results in Section 3.1 show that H trapping in the IA700 sample is dominated by sites with relatively low trapping energies (i.e. weak trapping sites). The determined desorption

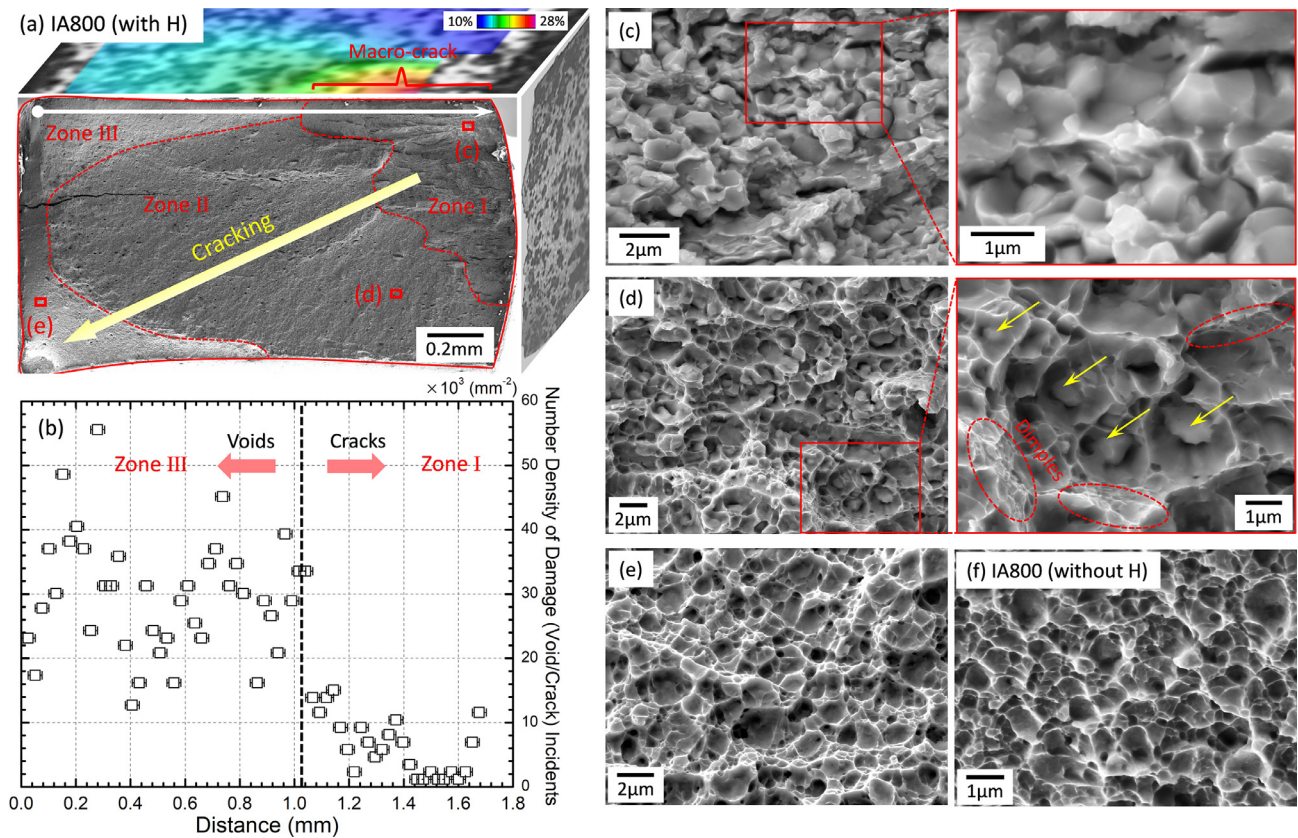


**Fig. 7.** (a) Overview fracture surface of the H pre-charged IA800 sample, showing three zones containing different fracture features. The DIC strain map measured for the same specimen just before fracture is also added in this figure, aiming to show the position of the macroscopic crack (the images are organized in a pseudo 3-dimensional form); (b) The distribution of damage (voids or cracks) along the cross-section of the same tensile specimen in (a), measured by BSE imaging at regions just beneath the DIC measured surface and adjacent to the fracture surface (roughly corresponding to the white arrow marked in (a)); (c)–(e) Magnified images taken from the rectangular frames in (a), showing the fracture features in different zones; (f) The fracture surface of the non-charged IA800 sample. (For interpretation of the references to color in this figure legend, the reader is referred to the web version of this article.)

activation energy ( $\sim 20$  kJ/mol) implies that these sites are dislocations/grain boundaries in the ferrite. This agrees well with the fact that the IA700 sample with its higher ferrite grain boundary area (due to higher ferrite fraction and smaller grain size, Table 1) and higher dislocation density takes up more H than the IA800 sample (Fig. 2(a) and Table 1).

In contrast for the IA800 sample, H is trapped not only at defects inside ferrite, but also at some stronger trapping sites as supported by the higher temperature desorption peaks (second and third peak in Fig. 2(c)) and their prevalence also after prolonged aging times (120 h). The  $E_A$  value determined for the second ( $\sim 40$  kJ/mol) and third peak ( $\sim 51$  kJ/mol) agree with those reported for H desorption from austenite ( $E_A = 40\text{--}55$  [37,38], determined by TDA) and from the  $\alpha$ - $\gamma$  interface ( $E_A = 50\text{--}57$  kJ/mol [15], determined by TDA), respectively. Hydrogen trapping in these two sites in the IA800 sample is supported by the high fraction of cracking events inside the austenite phase and at the  $\alpha$ - $\gamma/\alpha'$  interfaces (Fig. 9(a)).

The different H trapping behavior between the two samples can be explained in terms of their different phase percolation due to their different phase fractions. In the IA700 sample, the austenite fraction is low ( $\sim 26$  vol.%), and the dispersed austenite islands are embedded in the ferritic matrix. Since ferrite has a much higher H diffusivity than austenite [12–14], the fully connected three-dimensional ferritic network provides an efficient and fast path for H transport [13]. This is similar to the situation in duplex stainless steels where austenite islands are also embedded in ferrite. It was proposed for such steels [13,14] that the overall H transport was

mainly governed by H diffusion through the percolating ferrite phase and the embedded austenite can be circumvented, i.e. it does not principally interrupt the diffusion paths. This H transport behavior indicates that within a limited charging time (here 24 h), the amount of H that gets trapped at the  $\alpha$ - $\gamma$  phase boundary and inside the austenite might be limited. More importantly, the large number of dislocations inside the ferrite, especially the ones near phase boundaries, can effectively trap H and prevent it from diffusing into phase boundaries and austenite. The presence of a high density of GNDs near the  $\alpha$ - $\gamma$  interfaces in the non-deformed IA700 sample is directly observed by ECCI (Fig. 10(a)) and supported by the EBSD KAM map which shows a high local misorientation value inside ferrite near the phase boundaries (Fig. 10(b) and (c)).

In contrast to the prevalence of ferrite in the IA700 sample, in the IA800 sample the austenite dominates with a volume fraction of  $\sim 59$  vol.%, acting as matrix phase with embedded ferrite. Hence, no percolating fast H diffusion path exists through the ferrite, thus a higher fraction of the abundant H gets inevitably trapped at the  $\alpha$ - $\gamma$  interfaces and inside the austenite when the H migrates from the sample surface to the center during electrochemical charging. This topological effect thus reduces the effective diffusivity of H [50] and slows down the through-thickness diffusion of H. Therefore, in the IA800 sample, H-assisted cracking/fracture remains confined to the regions close to the side edges which are first loaded with H during charging (Zone I in Fig. 7(a)). The proposed microstructure-driven H distribution for the two types of microstructures is described schematically in Fig. 11.



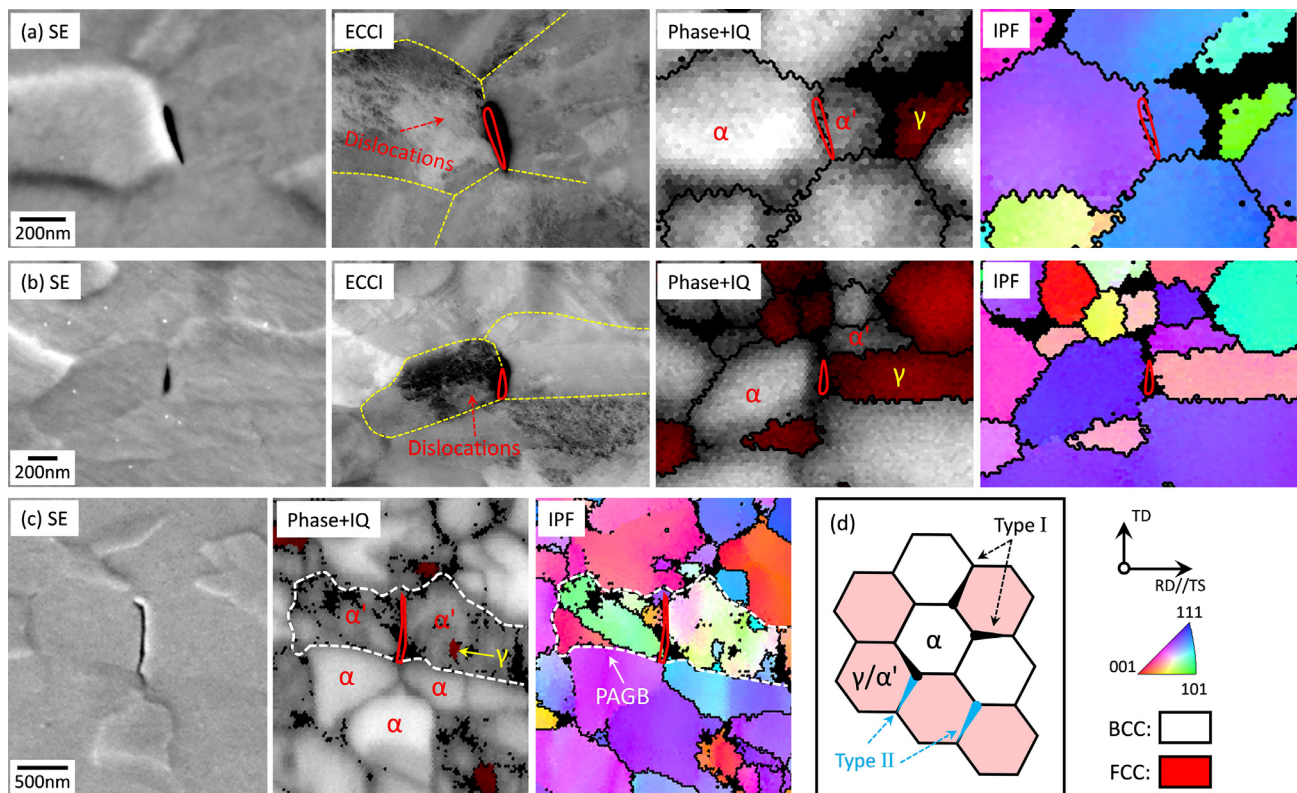


**Fig. 8.** Correlative secondary electron (SE) imaging, ECCI and EBSD results (including phase plus image quality (IQ) mapping and EBSD inverse pole figure (IPF)) taken from locations near the fracture surface of Zone I in the H pre-charged IA800 sample, showing typical nanoscaled cracks forming at (a) the ferrite and strain-induced  $\alpha'$ -martensite interface, (b) ferrite and austenite interface and (c) prior-austenite grain boundary (the SE images here serves to identify the cracks. PAGB represents prior-austenite grain boundary. Differentiating ferrite and  $\alpha'$ -martensite was based on the intensity of the EBSD IQ map and kernel average misorientation map (not presented here)); (d) Schematic illustration of two main cracking events in the H pre-charged IA800 sample. (For interpretation of the references to color in this figure legend, the reader is referred to the web version of this article.)

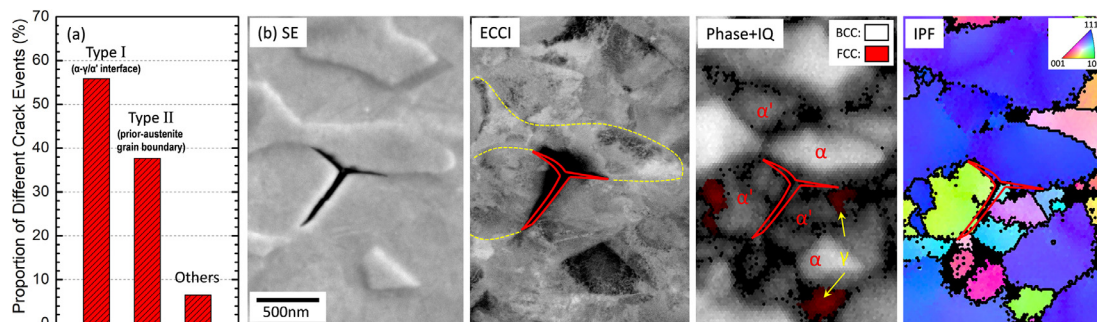


**Fig. 9.** (a) Statistical cracking analysis showing the proportion of different cracking events near the fracture surface of Zone I in the H pre-charged IA800 sample (data acquired from ~150 nano-/micro-cracks probed by SE imaging); (b) One typical example showing the nucleation of a crack at a triple junction followed by the simultaneous propagation along the  $\alpha$ - $\gamma$ / $\alpha'$  interface boundary and the prior-austenite grain boundary (IQ: EBSD image quality map; IPF: EBSD inverse pole figure).

It is worthwhile to mention that, given the complex microstructures of the investigated steels with their wide variety of potential trapping sites, revealing all the H trapping sites (especially the minor ones) remains highly challenging only by TDA results. It is thus not the main focus here. Mapping H trapping with higher resolution and fidelity in such ultrafine microstructures as the current ones would essentially require the combination of direct H imaging methods with a spatial resolution at the nanoscale (e.g. scanning Kelvin probe force microscopy and atom probe tomography [51]), which will be the subject of future studies. For the IA800 sample, although the determined values of  $E_A$  for each peak matches those reported in the literature, one might still argue that the analysis of different desorption peaks in this sample

is to some extent arbitrary because complex peak overlap effects might conceal a more complex trapping spectrum. However, here we mainly aim to show the difference in H trapping between the two types of microstructures, i.e. more H tends to be trapped in at least two additional strong trapping sites in the IA800 sample compared to the IA700 material. Except the trapping of H inside austenite and at  $\alpha$ - $\gamma$  interfaces, other well documented strong trapping sites (including iron-vacancy [16,35], microvoids [16,29] and inclusions [16]) are unlikely to play a dominant role in the IA800 microstructure, because the density of these sites is expected to be rather unaffected by the annealing treatment (for microvoids and inclusions) or even reduced in the IA800 sample (for vacancy) due to the more complete recrystallization [35,52].



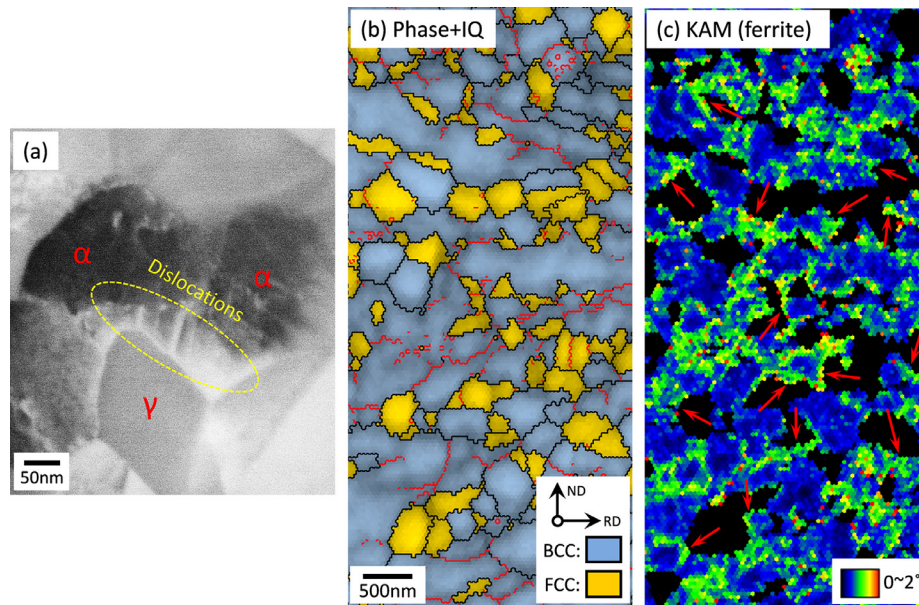


**Fig. 10.** (a) ECCI observation of the non-deformed IA700 sample, showing a high density of dislocations near the austenite-ferrite phase boundaries; (b) EBSD phase plus image quality (IQ) and (c) ferrite kernel average misorientation (KAM) mapping for the same sample in (a), showing a high value of local misorientations inside ferrite near the austenite-ferrite interfaces (some typical regions are marked by red arrows). (The black and red lines in (b) represents high and low angle interface boundaries, respectively. The austenite phase in (c) is shown in black color.) (For interpretation of the references to color in this figure legend, the reader is referred to the web version of this article.)

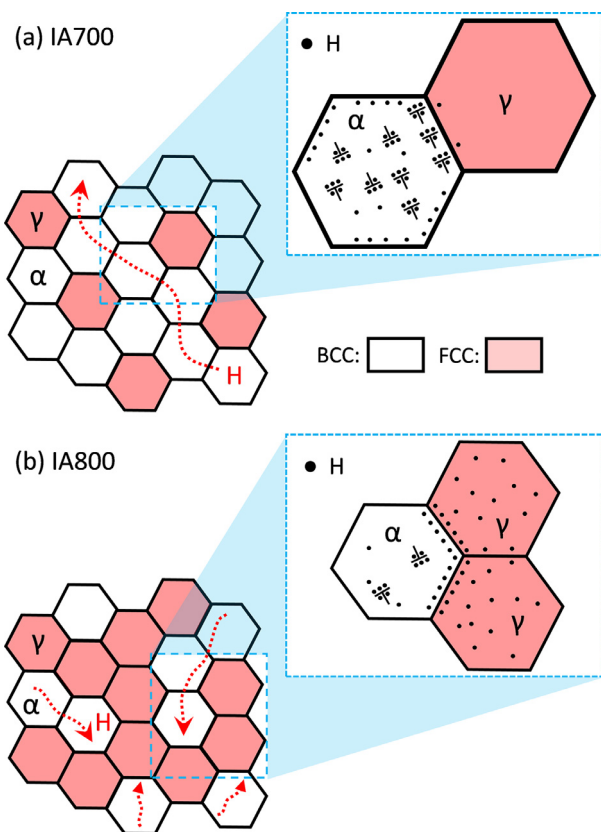


**Fig. 11.** Schematic sketch describing the microstructure-driven H distribution in (a) the IA700 sample and (b) the IA800 sample.

## 4.2. Hydrogen embrittlement micromechanisms

### 4.2.1. Sample IA700 with ferritic matrix

The H-charged IA700 sample exhibits a major dimple-type fracture surface (Fig. 4(b)), caused by void nucleation mainly at

the  $\alpha$ - $\gamma/\alpha'$  interfaces and their further growth and coalescence (Figs. 5 and 6). Results in Section 3.1 and the discussion in Section 4.1 show that in this sample, H is mainly trapped in defects inside ferrite rather than at other stronger trapping sites such as phase boundaries. Thus the cohesive strength of the  $\alpha$ - $\gamma$  interface is not much reduced in the H-charged specimen. This point is supported by the absence of damage propagation features along the phase boundaries and the intergranular fracture mode. The void nucleation at the phase boundaries in both the H-charged and non-charged specimens is thus explained by the high strain incompatibility and the resulting high local stress concentrations at the phase boundaries (Section 3.3.1). The quantitative damage analysis in Fig. 6 shows that the rate of void nucleation is remarkably increased by the presence of H, which leads to a higher total void fraction and early sample fracture. Fig. 5(c) shows that the presence of H in the IA700 sample does not promote damage formation inside the austenite or strain-induced martensite phase. This behavior clearly differs from the case of the IA800 sample, where a substantially high fraction of H-induced cracks occurs inside the strain-induced martensite (primarily along the prior-austenite grain boundaries, Fig. 9(a)). This difference supports our understanding that the amount of H trapped inside austenite in the IA700 sample should be only slight under the current charging conditions. Therefore, the role of strain-induced transformation in the IA700 sample mainly lies in its increasing effect on the fraction of fresh martensite and thus the degree of strain incompatibility. This influence should be the same for both, the non-charged and H pre-charged IA700 specimens.

The above-mentioned H influence on void nucleation can be explained in the framework of the HELP mechanism. The original formulation of this mechanism was based on elasticity theory [21,22]. It proposes that H forms a Cottrell-type atmosphere around dislocations and other elastic stress centers, providing an elastic shielding effect in which the interaction energy or elastic force between dislocations and obstacles is reduced [22]. An alternative explanation referred to as defectant concept was recently developed based on the extended version of the Gibbs adsorption isotherm [53–55]. The idea of this model is the reduction of the formation energy of

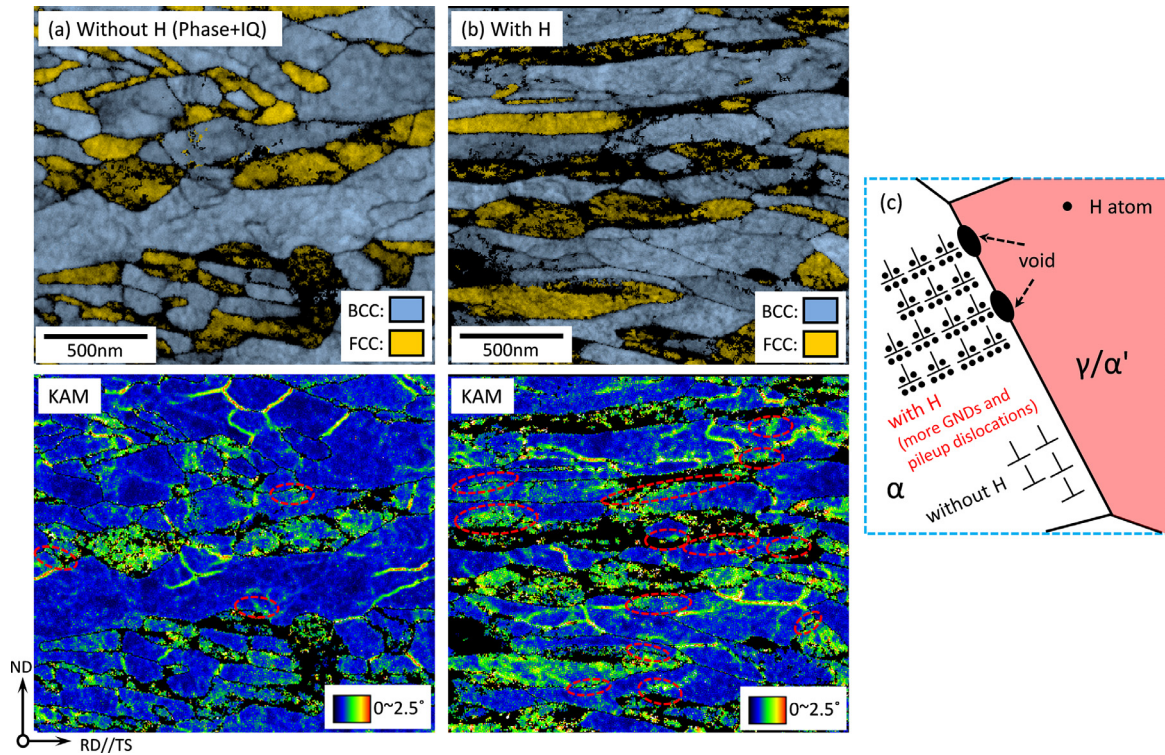


**Fig. 12.** Transmission Kikuchi diffraction (TKD) results showing the representative phase plus image quality (IQ) and the kernel average misorientation (KAM) mapping of the deformed IA700 sample (a) without H pre-charging and (b) with H pre-charging (the probing areas in the two samples are at the same local strain (~48%); some high local-misorientation areas inside ferrite near the phase boundaries are marked by elliptical frames); (c) Schematic sketch describing the dominant role of the HELP mechanism on void nucleation in the IA700 sample. (For interpretation of the references to color in this figure legend, the reader is referred to the web version of this article.)

dislocations in the presence of defactant solutes (e.g. H) [54,55]. The former model mainly focuses on H-enhanced dislocation mobility and the latter on H-promoted dislocation generation. Both models explain facilitated plastic flow (i.e. softening) induced by H, which has indeed been observed in some materials [23,53]. In this regard, the ferrite in the IA700 sample could have been effectively softened by the trapped H. This enlarges the local mechanical contrast between ferrite and the adjacent  $\gamma$ - $\alpha'$  mixed phase, especially at relatively high strain levels where most of the austenite has transformed into martensite. The degree of strain incompatibility is thus increased, which effectively promotes void nucleation at the phase boundaries. In order to check this scenario, we performed TKD experiments for the nanoscale imaging of the local misorientations in the deformed IA700 samples with and without H pre-charging. The probing areas of the two samples are at the same local strain (~48%). Representative results are shown in Fig. 12(a) and (b). We find that the H-charged sample exhibits a pronouncedly higher value of local misorientations inside the  $\alpha$  phase close to the phase boundaries (marked by elliptical frames) compared with the non-charged condition, which is a direct result of the higher strain incompatibility (thus more GNDs) due to the HELP effect in the ferrite. The dominant effect of the HELP mechanism on void nucleation is schematically shown in Fig. 12(c).

According to the H shielding theory [22], the HELP effect is only effective when the H atmospheres move together with the dislocations, which requires the applied strain rate to be relatively low. The critical strain rate ( $\dot{\epsilon}_c$ ) for dislocations to break away from their H atmospheres in ferrite can be written according to Cottrell [56–58]:

$$\dot{\epsilon}_c = \frac{4D\rho b}{R}$$

where  $D$  is the diffusion coefficient of H,  $\rho$  is the dislocation density,  $b$  is the magnitude of the Burgers vector and  $R$  is the effective

radius of the H atmosphere. The radius  $R$  is equal to  $E_b b/kT$  [58], where  $E_b$  is the binding energy between H and dislocations ( $E_b = E_A - E_{diff}$ ,  $E_{diff}$  is taken as 7.6 kJ/mol [29]) and  $k$  is the Boltzmann constant. Since the ferrite in the IA700 sample has a similar dislocation density as the tempered martensite ( $\rho = \sim 10^{14} \text{ m}^{-2}$  [59]), the value of  $D$  is here also assumed to be similar to that in tempered martensite ( $D = \sim 5 \times 10^{-11} \text{ m}^2/\text{s}$  [60]). The value of  $\dot{\epsilon}_c$  is thus estimated to be around  $4 \times 10^3 \text{ s}^{-1}$ . Below this critical strain rate, the H atmospheres, once formed around dislocations in ferrite during charging, should always be capable to move together with the dislocations, permanently shielding them as described by the HELP effect. For the IA700 sample, we have shown that the H-assisted early fracture is due to the significantly increased void nucleation rate at the phase boundaries, driven by the H-enhanced dislocation activity inside ferrite. Such a H-assisted failure process is not associated with the buildup of local H concentration at the high stress concentrated areas (e.g. near the macro/micro-crack tips), i.e. H diffusion is not necessarily required. This indicates that the H-assisted fracture of the IA700 sample is not sensitive to the change of the strain rate, as long as the applied strain rate is within the range where the HELP effect is operative (below  $4 \times 10^3 \text{ s}^{-1}$ ). This strain rate insensitivity of the HE susceptibility in the IA700 sample is validated in Fig. 13(a), in which a similar ductility degradation due to the presence of H is observed when the applied strain rate is increased from  $8 \times 10^{-5} \text{ s}^{-1}$  (total elongation loss 8.5%, Table 2) to  $5 \times 10^{-3} \text{ s}^{-1}$  (associated with a total elongation loss 8.2%). This observation is different from previous reports on ferritic [61], high Mn austenitic [62] and medium Mn austenite-ferrite steels [1], where a higher HE susceptibility is normally observed at lower applied strain rates in H pre-charged specimens. The finding provides an additional indirect evidence supporting the dominant role of the HELP mechanism in the IA700 sample.



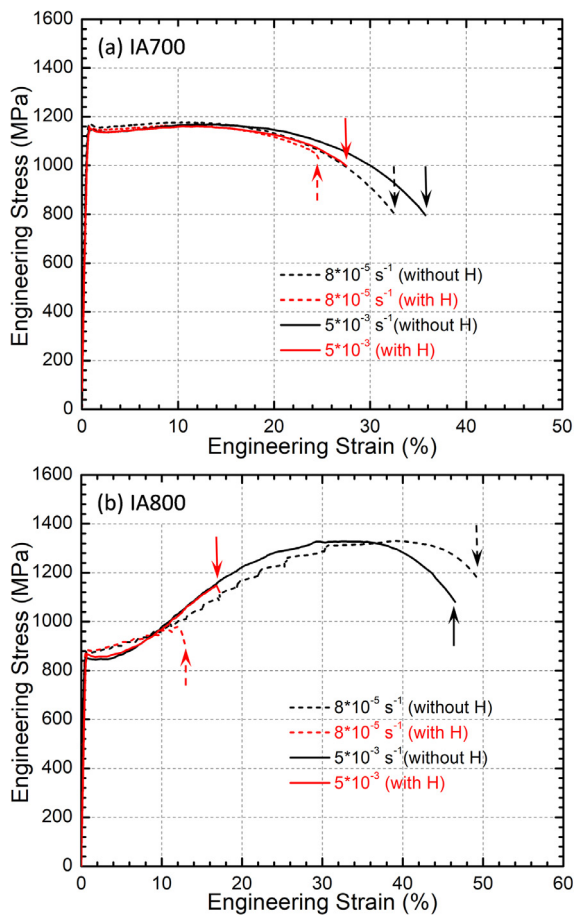


**Fig. 13.** The effect of applied strain rate on the hydrogen embrittlement susceptibility for (a) the IA700 sample and (b) the IA800 sample. (The H pre-charging condition was the same for all the samples tested at different strain rates.)

#### 4.2.2. Sample IA800 with austenitic matrix

The damage analysis presented in Section 3.3.2 shows that failure of the H-charged IA800 sample is mainly driven by H-assisted crack nucleation and propagation along both, the  $\alpha$ - $\gamma$ / $\alpha'$  interfaces and the prior-austenite grain boundaries, which leads to a percolating intergranular fracture surface already during the early fracture stage (Zone I, Fig. 7). A reduction of the cohesive strength of the interfaces is essentially required to support this fracture mode. Otherwise, the nucleated cracks would tend to be blunted rapidly by dislocation emission at the crack tips and develop into voids, which is the case observed in the H-charged and non-charged IA700 samples and the non-charged IA800 sample. These observations show that the HEDE mechanism is likely to be the dominant cause for the catastrophic fracture of the H-charged IA800 sample.

Discussion in Section 4.1 shows that some H in the pre-charged IA800 sample is trapped at the  $\alpha$ - $\gamma$  interface and inside the austenite. It was reported before that the interaction between H and austenite grain boundaries is weak, with a binding energy around 0–15 kJ/mol [63,64]. This value is much smaller than the activation energy for H diffusion in the austenite lattice (above 40 kJ/mol [37,38,65]). This suggests that the H concentration at austenite grain boundaries in equilibrium should be very small. The low diffusivity of H in austenite also reduces H migration to austenite grain boundaries. The negligible role of the austenite grain boundaries on the trapping of H has been reported by Mine et al. [64] and Sun et al. [65] in different austenitic stainless steels. Then if the initially trapped H is assumed to be responsible for

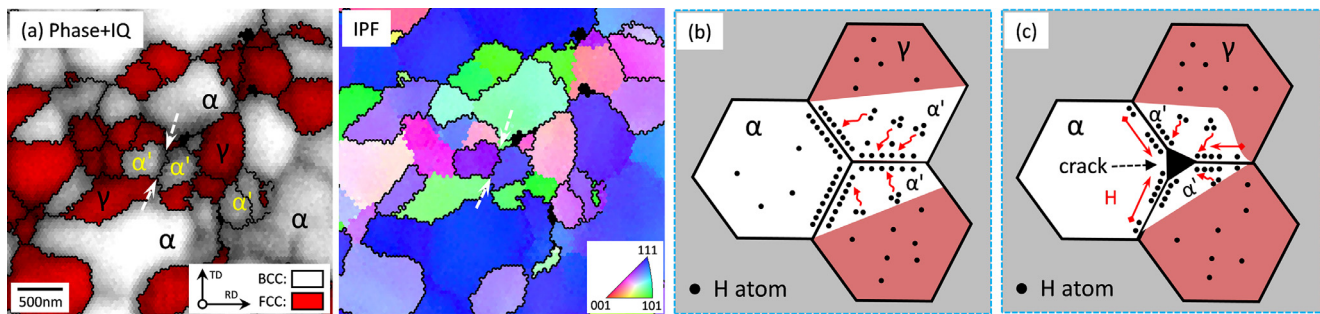
interface decohesion, it is challenging to explain why such a high proportion of cracks is located at prior-austenite grain boundaries (Fig. 9(a)). Therefore, H migration or its redistribution should most likely occur during the early plastic deformation stage (prior to crack nucleation) and during the propagation stage of nano-/micro-cracks, driven by the local change of the microstructure and stress concentration.

Fig. 3(d) shows that strain-induced  $\alpha'$ -martensite formation occurs already from the beginning of tensile testing for the H-charged IA800 sample. At the point of fracture (~13% strain), nearly 20 vol.% martensite has been formed. The EBSD results for one typical region at this strain level are shown in Fig. 14(a). For certain grain boundaries (marked by arrows in Fig. 14(a)), the adjacent austenite has been entirely transformed to martensite, which means that the original FCC-FCC interface has now become a BCC-BCC interface. The austenite-to-martensite transformation would leave H in a super-saturated and highly diffusible state [1], allowing H atoms to rapidly migrate to the nearest interfaces and decrease their cohesive strength. This process is demonstrated schematically in Fig. 14(b). In the other scenario (described in Fig. 14(c)), cracks nucleate before martensite forms. Triple junctions composed of both  $\alpha$ - $\gamma$  and  $\gamma$ - $\gamma$  interfaces can act as preferable crack nucleation sites due to the displacement mismatch and the resulting high stress concentrations [66]. A typical example for this has been shown in Fig. 9(b). The formation of cracks abruptly increases the local stress and strain near the crack tips, triggering the neighboring austenite to transform to martensite, followed by H migration to the interfaces near the crack tips. The nucleated cracks would then tend to propagate along these decorated interfaces with their higher accumulated H concentration and lower cohesive strength. Both of the above processes (Fig. 14(b) and (c)) suggest that the H-assisted cracking in the IA800 sample is highly influenced by H migration during deformation. This mechanism is also reflected by the dependence of the HE susceptibility on the applied strain rates. The tensile curves of both H-charged and non-charged IA800 samples at different strain rates are shown in Fig. 13(b). A clear increase of HE resistance is observed with increasing applied strain rate (total elongation loss: 38.2% at  $8 \times 10^{-5} \text{ s}^{-1}$  vs. 29.3% at  $5 \times 10^{-3} \text{ s}^{-1}$ ).

#### 4.3. Microstructural factors influencing hydrogen embrittlement in medium Mn steels and implications on future microstructural design

One important feature of medium Mn steels compared with other high strength steels is the high degree of microstructural flexibility. While this advantage provides a large scope of microstructural design options towards improved mechanical properties, it significantly alters the HE behavior. Here we show that the two samples investigated with their 'extreme', i.e. upper and lower bound microstructural conditions, have very different resistance to HE with different prevalent embrittling mechanisms (i.e. HELP in the IA700 sample and HEDE in the IA800 sample). This difference is related to the variation of the H distribution controlled by the microstructure. It is commonly reported that higher strength in steels increases the susceptibility to HE [16]. This trend is clearly not true for the current study. The IA700 sample with a much higher yield strength exhibits a much better HE resistance than the IA800 sample (Fig. 2(a) and Table 2). Previous literature on TRIP-aided metastable stainless steels [12] and medium Mn steels [1,9] claimed that austenite to  $\alpha'$ -martensite transformation could effectively deteriorate the HE resistance, due to the resulting high local stress and increased local H diffusivity [1]. However, we observe that this deterioration effect is only pronounced in the IA800 sample where H is initially trapped inside the austenite.





**Fig. 14.** (a) EBSD phase plus image quality (IQ) mapping and inverse pole figure (IPF) for one typical region in the H-charged IA800 sample with a local strain of ~13%, representing the microstructure just prior to fracture (one prior-austenite grain boundary is marked by arrows); Schematic sketch describing the H migration behavior during (b) the early plastic deformation stage when strain-induced martensite forms prior to crack nucleation and (c) the crack propagation stage.

Therefore, if H is not saturated throughout the whole material,<sup>1</sup> the microstructure-driven H distribution governed by the phase fraction and percolation should be a first-order effect influencing HE in medium Mn steels.

On the other hand, the two investigated samples share a common feature. Both show a remarkably high proportion of H-assisted damage at the  $\alpha$ - $\gamma/\alpha'$  phase boundaries (Figs. 5(c) and 9(a)), no matter whether this is due to a direct H-induced decrease of cohesive strength (IA800 sample) or due to the H-assisted local plasticity in ferrite and the resulted high strain incompatibility (IA700 sample). Observing this high proportion of damages at phase boundaries is plausible in the sense that the phase boundary is the major type of planar defects in medium Mn steels due to the material's duplex-type microstructure (Fig. 1). Such a critical role of phase boundaries on H-assisted damage formation has not been revealed in depth before and is thus highlighted here. Further engineering of the structural nature and compositional decoration of phase boundaries could therefore be a pathway for rendering medium Mn steels more resistant to HE embrittlement.

Another strategy for H-resistant microstructural design inspired from this study lies in decelerating the effective long-range bulk H diffusion via interrupting the percolating fast H diffusion path, which can be achieved by the alternation of phase percolation. In this study, the change of phase percolation is simply realized by increasing the phase fraction of austenite to a sufficient amount (i.e. above the percolation threshold [68]). Other approaches such as a spatially confined phase transformation at the grain boundary of the parent phase can also effectively influence the phase percolation. These approaches are not only restricted in the current medium Mn steels. They can in principle be applied also in other multiphase materials such as carbide-free bainitic steels [50]. However, it has been discussed in Section 4.1 that, although the change of phase percolation (here from ferrite to austenite percolation) can decelerate the bulk H diffusion, it can also enhance the tendency of H trapping at the phase boundaries due to the disappearance of fast H diffusion path. This might bring some detrimental effects as shown in the case of the IA800 sample where the phase boundaries are directly embrittled by the presence of H. Therefore, the application of this strategy must carefully balance the beneficial and detrimental factors resulting from phase percolation alternation.

## 5. Conclusions

The present study investigated the HE mechanisms of two austenite-ferrite medium Mn steel samples with very different (upper and lower bound) phase conditions. The H trapping behavior, H-assisted damage evolution and H-assisted local plasticity/dislocation behavior were systematically studied. The main conclusions are:

- (1) The IA700 sample was characterized by a ferritic matrix (~74 vol.%  $\alpha$ ) with embedded austenite, very high austenite mechanical stability (absence of strain-induced martensite during uniform straining) and a high dislocation density in ferrite, whereas the IA800 sample featured an austenitic matrix (~59 vol.%  $\gamma$ ) with embedded ferrite, low austenite stability (strain-induced martensite transformation occurs immediately after yielding) and a fully recrystallized microstructure. Despite much higher yield strength, higher defect density and much stronger H uptake capacity for the IA700 sample, it showed a significantly higher resistance to HE compared to the IA800 sample. The degradation of total elongation due to the presence of H was 8.5% and 38.2% for the IA700 and IA800 sample, respectively.
- (2) H trapping in the IA700 sample was dominated by relatively weak trapping sites, i.e. dislocations/grain boundaries in ferrite. The presence of H in this sample mainly increased the rate of void nucleation at the  $\alpha$ - $\gamma/\alpha'$  phase boundaries, which resulted in a higher total damage fraction and early sample fracture. This phenomenon was explained in the framework of the HELP mechanism: H enhanced the local plastic flow in ferrite thus increasing the mechanical contrast and the strain incompatibility between ferrite and the neighboring  $\gamma$ - $\alpha'$  mixed phase. The increased strain incompatibility (thus more GNDs) was directly validated by nanoscale imaging of local misorientations near the phase boundaries. The dominant role of the HELP mechanism in the IA700 sample was also indirectly supported by its insensitivity of HE resistance to applied strain rates.
- (3) For the IA800 sample, some amount of H was trapped at stronger trapping sites, including  $\alpha$ - $\gamma$  phase boundaries and austenite. This initially trapped H and phase transformation-induced H migration to interfaces during deformation resulted in H-assisted crack nucleation and propagation along the  $\alpha$ - $\gamma/\alpha'$  interfaces and the prior-austenite grain boundaries, which led to an intergranular typed fracture surface at the early fracture zone. This process implied a dominant role of the HEDE mechanism. The dependence of H-assisted fracture on H migration in the IA800 sample was supported by its higher sensitivity of HE susceptibility to applied strain rates.
- (4) The different H migration and trapping behavior between the two investigated types of samples was mainly attributed

<sup>1</sup> Based on the reported H diffusion coefficient ( $D = 10^{-15} \sim 10^{-13} \text{ m}^2/\text{s}$  [67]) in duplex stainless steels with around 40–50% austenite, the diffusion distance ( $\sim (Dt)^{0.5}$ ) of H at room temperature after 10 days ( $t = 864000 \text{ s}$ ) is only about 30–300  $\mu\text{m}$ . Note that the value of  $D$  could be even smaller in medium Mn steels due to the higher density of interfaces and easily achieved austenite percolation. This calculation indicates that full H saturation in medium Mn steels is difficult to achieve.

to the different phase fractions and their percolation. Such microstructure-driven H distribution had a crucial influence on HE susceptibility and fundamental HE micromechanisms in medium Mn steels. Tailoring phase fraction, interface state and percolation thus provides a possibility to achieve a high strength level at low HE susceptibility (i.e. like in the case of the IA700 sample). This information provides significant insights for future microstructural design towards higher HE resistance in high-strength steels.

### Declaration of Competing Interest

The authors declare that they have no known competing financial interests or personal relationships that could have appeared to influence the work reported in this paper.

### Acknowledgments

K. Angenendt and M. Adamek at the Max-Planck-Institut für Eisenforschung GmbH is acknowledged for the support of the TKD and dilatometry experiments. M. Elkot is acknowledged for the helpful discussion regarding H diffusion. The authors acknowledge Prof. S. Yue from McGill University and Dr. F. Fazeli and Dr. C. Scott from CanmetMATERIALS, Canada, for providing the materials. B. Sun gratefully acknowledges the research fellowship provided by the Alexander von Humboldt Foundation.

### Supplementary materials

Supplementary material associated with this article can be found, in the online version, at doi:[10.1016/j.actamat.2019.11.029](https://doi.org/10.1016/j.actamat.2019.11.029).

### References

- [1] J.H. Ryu, Y.S. Chun, C.S. Lee, H. Bhadeshia, D.W. Suh, Effect of deformation on hydrogen trapping and effusion in TRIP-assisted steel, *Acta Mater* 60 (2012) 4085–4092.
- [2] J. Han, J.H. Nam, Y.K. Lee, The mechanism of hydrogen embrittlement in intercritically annealed medium Mn trip steel, *Acta Mater* 113 (2016) 1–10.
- [3] Q. Han, Y. Zhang, L. Wang, Effect of annealing time on microstructural evolution and deformation characteristics in 10Mn1.5Al trip steel, *metall. Mater. Trans. A* 46 (2015) 1917–1926.
- [4] B. Sun, F. Fazeli, C. Scott, B. Guo, C. Aranas Jr, X. Chu, M. Jahazi, S. Yue, Microstructural characteristics and tensile behavior of medium manganese steels with different manganese additions, *Mater. Sci. Eng., A* 729 (2018) 496–507.
- [5] S. Lee, B.C. De Cooman, On the selection of the optimal intercritical annealing temperature for medium mn trip steel, *Metall. Mater. Trans. A* 44 (2013) 5018–5024.
- [6] B. Sun, Y. Ma, N. Vanderesse, R.S. Varanasi, W. Song, P. Bocher, D. Ponge, D. Raabe, Macroscopic to nanoscopic in situ investigation on yielding mechanisms in ultrafine grained medium Mn steels: role of the austenite-ferrite interface, *Acta Mater* 178 (2019) 10–25.
- [7] B. Sun, R. Ding, N. Brodusch, H. Chen, B. Guo, F. Fazeli, D. Ponge, R. Gauvin, S. Yue, Improving the ductility of ultrahigh-strength medium mn steels via introducing pre-existed austenite acting as a “reservoir” for Mn atoms, *Mater. Sci. Eng., A* 749 (2019) 235–240.
- [8] B. He, M. Huang, Strong and ductile medium mn steel without transformation-induced plasticity effect, *Mater. Res. Letters* 6 (2018) 365–371.
- [9] C. Shao, W. Hui, Y. Zhang, X. Zhao, Y. Weng, Effect of intercritical annealing time on hydrogen embrittlement of warm-rolled medium Mn steel, *Mater. Sci. Eng., A* 726 (2018) 320–331.
- [10] B. Sun, Processing, microstructure and mechanical behavior of medium manganese steels, in: *Proceedings of the Department of Mining and Materials Engineering*, McGill University, Montreal, 2017.
- [11] Y. Zhang, W. Hui, J. Wang, M. Lei, X. Zhao, Enhancing the resistance to hydrogen embrittlement of al-containing medium-Mn steel through heavy warm rolling, *Scripta Mater* 165 (2019) 15–19.
- [12] T. Perng, C. Altstetter, Comparison of hydrogen gas embrittlement of austenitic and ferritic stainless steels, *Metall. Trans. A* 18 (1987) 123–134.
- [13] A. Turnbull, R. Hutchings, Analysis of hydrogen atom transport in a two-phase alloy, *Mater. Sci. Eng., A* 177 (1994) 161–171.
- [14] E. Owczarek, T. Zakroczyński, Hydrogen transport in a duplex stainless steel, *Acta Mater* 48 (2000) 3059–3070.
- [15] E. Dabab, V. Lisitsyn, D. Eliezer, Performance of hydrogen trapping and phase transformation in hydrogenated duplex stainless steels, *Mater. Sci. Eng., A* 527 (2010) 4851–4857.
- [16] H.K.D.H. Bhadeshia, Prevention of hydrogen embrittlement in steels, *ISIJ Int* 56 (2016) 24–36.
- [17] B. Sun, D. Palanisamy, D. Ponge, B. Gault, F. Fazeli, C. Scott, S. Yue, D. Raabe, Revealing fracture mechanisms of medium manganese steels with and without delta-ferrite, *Acta Mater* 164 (2019) 683–696.
- [18] B. Sun, F. Fazeli, C. Scott, X. Yan, Z. Liu, X. Qin, S. Yue, Critical role of strain partitioning and deformation twinning on cracking phenomenon occurring during cold rolling of two duplex medium manganese steels, *Scripta Mater* 130 (2017) 49–53.
- [19] A.R. Troiano, The role of hydrogen and other interstitials in the mechanical behavior of metals, *Trans. Am. Soc. Metals* 52 (1960) 54–80.
- [20] R. Oriani, A mechanistic theory of hydrogen embrittlement of steels, *Berichte der Bunsengesellschaft für physikalische Chemie* 76 (1972) 848–857.
- [21] I. Robertson, The effect of hydrogen on dislocation dynamics, *Eng. Fract. Mech.* 64 (1999) 649–673.
- [22] H.K. Birnbaum, P. Sofronis, Hydrogen-enhanced localized plasticity—a mechanism for hydrogen-related fracture, *Mater. Sci. Eng., A* 176 (1994) 191–202.
- [23] C. Beacheam, A new model for hydrogen-assisted cracking (hydrogen “embrittlement”), *Metall. Mater. Trans. B* 3 (1972) 441–455.
- [24] S. Lynch, Hydrogen embrittlement (HE) phenomena and mechanisms, in: V.S. Raja, T. Shoji (Eds.), *Stress Corrosion Cracking*, Woodhead Publishing, 2011, pp. 90–130.
- [25] B. Sun, F. Fazeli, C. Scott, N. Brodusch, R. Gauvin, S. Yue, The influence of silicon additions on the deformation behavior of austenite-ferrite duplex medium manganese steels, *Acta Mater* 148 (2018) 249–262.
- [26] S.V. Merzlikin, S. Borodin, D. Vogel, M. Rohwerder, Ultra high vacuum high precision low background setup with temperature control for thermal desorption mass spectroscopy (TDA-MS) of hydrogen in metals, *Talanta* 136 (2015) 108–113.
- [27] H.E. Kissinger, Reaction kinetics in differential thermal analysis, *Anal. Chem.* 29 (1957) 1702–1706.
- [28] R. Kirchheim, Bulk diffusion-controlled thermal desorption spectroscopy with examples for hydrogen in iron, *Metall. Mater. Trans. A* 47 (2016) 672–696.
- [29] W. Choo, J.Y. Lee, Thermal analysis of trapped hydrogen in pure iron, *Metall. Trans. A* 13 (1982) 135–140.
- [30] I. Gutierrez-Urrutia, S. Zaefferer, D. Raabe, Electron channeling contrast imaging of twins and dislocations in twinning-induced plasticity steels under controlled diffraction conditions in a scanning electron microscope, *Scripta Mater* 61 (2009) 737–740.
- [31] S. Zaefferer, N.N. Elhami, Theory and application of electron channelling contrast imaging under controlled diffraction conditions, *Acta Mater* 75 (2014) 20–50.
- [32] E. Breitbarth, S. Zaefferer, F. Archie, M. Besel, D. Raabe, G. Requena, Evolution of dislocation patterns inside the plastic zone introduced by fatigue in an aged aluminium alloy AA2024-T3, *Mater. Sci. Eng., A* 718 (2018) 345–349.
- [33] M. Koyama, C.C. Tasan, E. Akiyama, K. Tsuzaki, D. Raabe, Hydrogen-assisted decohesion and localized plasticity in dual-phase steel, *Acta Mater* 70 (2014) 174–187.
- [34] F. Wei, T. Hara, K. Tsuzaki, Precise determination of the activation energy for desorption of hydrogen in two Ti-added steels by a single thermal-desorption spectrum, *Metall. Mater. Trans. B* 35 (2004) 587–597.
- [35] W. Krieger, S.V. Merzlikin, A. Bashir, A. Szczepaniak, H. Springer, M. Rohwerder, Spatially resolved localization and characterization of trapped hydrogen in zero to three dimensional defects inside ferritic steel, *Acta Mater* 144 (2018) 235–244.
- [36] J. Ronevich, B. De Cooman, J. Speer, E. De Moor, D. Matlock, Hydrogen effects in prestrained transformation induced plasticity steel, *Metall. Mater. Trans. A* 43 (2012) 2293–2301.
- [37] S. Ningshen, M. Uhlemann, F. Schneider, H. Khatak, Diffusion behaviour of hydrogen in nitrogen containing austenitic alloys, *Corros. Sci.* 43 (2001) 2255–2264.
- [38] Y. Park, I. Maroef, A. Landau, D. Olson, Retained austenite as a hydrogen trap in steel welds, *Welding J.* 81 (2002) 27–35.
- [39] T. Yokota, T. Shiraga, Evaluation of hydrogen content trapped by vanadium precipitates in a steel, *ISIJ Int* 43 (2003) 534–538.
- [40] P. Jacques, Q. Furnemont, T. Pardoen, F. Delannay, On the role of martensitic transformation on damage and cracking resistance in TRIP-assisted multiphase steels, *Acta Mater* 49 (2001) 139–152.
- [41] B. Sun, N. Vanderesse, F. Fazeli, C. Scott, J. Chen, P. Bocher, M. Jahazi, S. Yue, Discontinuous strain-induced martensite transformation related to the portevin-le chatelier effect in a medium manganese steel, *Scripta Mater* 133 (2017) 9–13.
- [42] S.J. Lee, J. Kim, S.N. Kane, B.C. De Cooman, On the origin of dynamic strain aging in twinning-induced plasticity steels, *Acta Mater* 59 (2011) 6809–6819.
- [43] E. Rizzi, P. Hähner, On the portevin-le chatelier effect: theoretical modeling and numerical results, *Int. J. Plast.* 20 (2004) 121–165.
- [44] M. Ashby, The deformation of plastically non-homogeneous materials, *The Philosoph. Mag. A J. Theoret. Exper. Appl. Phys.* 21 (1970) 399–424.
- [45] C. Landron, O. Bouaziz, E. Maire, J. Adrien, Characterization and modeling of void nucleation by interface decohesion in dual phase steels, *Scripta Mater* 63 (2010) 973–976.
- [46] A. Helbert, X. Feaugas, M. Clavel, Effects of microstructural parameters and back stress on damage mechanisms in  $\alpha/\beta$  titanium alloys, *Acta Mater* 46 (1998) 939–951.

- [47] E. Maire, O. Bouaziz, M. Di Michiel, C. Verdu, Initiation and growth of damage in a dual-phase steel observed by X-ray microtomography, *Acta Mater* 56 (2008) 4954–4964.
- [48] D. Fabrègue, C. Landron, O. Bouaziz, E. Maire, Damage evolution in twip and standard austenitic steel by means of 3D x ray tomography, *Mater. Sci. Eng., A* 579 (2013) 92–98.
- [49] H.Y. Yu, S.M. Lee, J.H. Nam, S.J. Lee, D. Fabrègue, M.H. Park, N. Tsuji, Y.K. Lee, Post-uniform elongation and tensile fracture mechanisms of fe-18mn-0.6c-xal twinning-induced plasticity steels, *Acta Mater.* 131 (2017) 435–444.
- [50] L. Fielding, E.J. Song, D.K. Han, H. Bhadeshia, D.-W. Suh, Hydrogen diffusion and the percolation of austenite in nanostructured bainitic steel, *Proc. R. Soc. A* 470:20140108.
- [51] M. Koyama, M. Rohwerder, C.C. Tasan, A. Bashir, E. Akiyama, K. Takai, D. Raabe, K. Tsuzaki, Recent progress in microstructural hydrogen mapping in steels: quantification, kinetic analysis, and multi-scale characterisation, *Mater. Sci. Technol.* 33 (2017) 1481–1496.
- [52] U. Holzwarth, A. Barbieri, S. Hansen-Illzhöfer, P. Schaaff, M. Haaks, Positron annihilation studies on the migration of deformation induced vacancies in stainless steel aisi 316L, *Appl. Phys. A* 73 (2001) 467–475.
- [53] A. Barnoush, H. Vehoff, Recent developments in the study of hydrogen embrittlement: hydrogen effect on dislocation nucleation, *Acta Mater* 58 (2010) 5274–5285.
- [54] R. Kirchheim, Reducing grain boundary, dislocation line and vacancy formation energies by solute segregation. I. theoretical background, *Acta Mater* 55 (2007) 5129–5138.
- [55] R. Kirchheim, Reducing grain boundary, dislocation line and vacancy formation energies by solute segregation: II. experimental evidence and consequences, *Acta Mater* 55 (2007) 5139–5148.
- [56] A.H. Cottrell, *Dislocations and Plastic Flow in Crystals*, Clarendon Press, Oxford, 1953.
- [57] A. Kimura, H.K. Birnbaum, Anomalous strain rate dependence of the serrated flow in ni-h and ni-c-h alloys, *Acta Metallurgica et Materialia* 38 (1990) 1343–1348.
- [58] P. McCormick, A model for the portevin-le chatelier effect in substitutional alloys, *Acta Metall* 20 (1972) 351–354.
- [59] S. Takebayashi, T. Kunieda, N. Yoshinaga, K. Ushioda, S. Ogata, Comparison of the dislocation density in martensitic steels evaluated by some X-ray diffraction methods, *ISIJ Int* 50 (2010) 875–882.
- [60] S. Frappart, X. Feaugas, J. Creus, F. Thebault, L. Delattre, H. Marchebois, Study of the hydrogen diffusion and segregation into fe-c-mo martensitic hsla steel using electrochemical permeation test, *J. Phys. Chem. Solids* 71 (2010) 1467–1479.
- [61] T. Doshida, K. Takai, Dependence of hydrogen-induced lattice defects and hydrogen embrittlement of cold-drawn pearlitic steels on hydrogen trap state, temperature, strain rate and hydrogen content, *Acta Mater* 79 (2014) 93–107.
- [62] B. Bal, M. Koyama, G. Gerstein, H. Maier, K. Tsuzaki, Effect of strain rate on hydrogen embrittlement susceptibility of twinning-induced plasticity steel pre-charged with high-pressure hydrogen gas, *Int. J. Hydrogen Energy* 41 (2016) 15362–15372.
- [63] E.J. Song, *Hydrogen Desorption in Steels*, Graduate Institute of Ferrous Technology, Pohang University of Science and Technology, 2015.
- [64] Y. Mine, Z. Horita, Hydrogen effects on ultrafine-grained steels processed by high-pressure torsion, *Mater. Trans* 53 (2012) 773–785.
- [65] S. Xiukui, X. Jian, L. Yiyi, Hydrogen permeation behaviour in austenitic stainless steels, *Mater. Sci. Eng., A* 114 (1989) 179–187.
- [66] S. Kobayashi, T. Inomata, H. Kobayashi, S. Tsurekawa, T. Watanabe, Effects of grain boundary and triple junction-character on intergranular fatigue crack nucleation in polycrystalline aluminum, *J. Mater. Sci.* 43 (2008) 3792–3799.
- [67] V. Olden, A. Saai, L. Jemblie, R. Johnsen, FE simulation of hydrogen diffusion in duplex stainless steel, *Int. J. Hydrogen Energy* 39 (2014) 1156–1163.
- [68] L. Priester, *Grain Boundaries: From Theory to Engineering*, Springer, Netherlands, 2013, doi:10.1007/978-94-007-4969-6.